A&A, 708, A380 (2026)
https://doi.org/10.1051/0004-6361/202556795

Astronomy & Astrophysics

The asymmetric structure of the inner disc around HD 142527 A with VLTI/MATISSE

M. B. Scheuck[1,2,⋆], R. van Boekel[1], Th. Henning[1], P. A. Boley[1], J. Varga[3], A. Matter[4], A. Penzlin[5], J. H. Leftley[4], L. van Haastere[6], K. Perraut[7], L. Labadie[8], M. Min[9,10], J. P. Berger[7], L. B. F. M. Waters[10,11], S. Zieba[12], B. Lopez[4], F. Lykou[3], J.-C. Augereau[7], P. Cruzalèbes[4], W. C. Danchi[13], V. Gámez Rosas[14], M. Hogerheijde[6], M. Letessier[7], J. Scigliuto[4], G. Weigelt[15], S. Wolf[16], and the MATISSE and GRAVITY collaborations

[1] Max-Planck-Institut für Astronomie, Königstuhl 17, 69117 Heidelberg, Germany
[2] Fakultät für Physik und Astronomie, Universität Heidelberg, Im Neuenheimer Feld 226, 69120 Heidelberg, Germany
[3] HUN-REN Research Centre for Astronomy and Earth Sciences, Konkoly Observatory, MTA Centre of Excellence, KonkolyThege Miklós út 15-17., 1121 Budapest, Hungary
[4] Laboratoire Lagrange, Université Côte d'Azur, Observatoire de la Côte d'Azur, CNRS, Boulevard de l'Observatoire, CS 34229, 06304 Nice Cedex 4, France
[5] Ludwig-Maximilians-Universität München, Universitäts-Sternwarte, Scheinerstr. 1, 81679 München, Germany
[6] Leiden Observatory, Leiden University, PO Box 9513, 2300 RA, Leiden, The Netherlands
[7] Univ. Grenoble Alpes, CNRS, IPAG, 38000 Grenoble, France
[8] I. Physikalisches Institut, Universität zu Köln, Zülpicher Str. 77, 50937 Köln, Germany
[9] Anton Pannekoek Institute for Astronomy, University of Amsterdam, Science Park 904, 1098XH Amsterdam, The Netherlands
[10] SRON Netherlands Institute for Space Research, Niels Bohrweg 4, 2333 CA Leiden, The Netherlands
[11] Institute for Mathematics, Astrophysics and Particle Physics, Radboud University, PO Box 9010, MC 62 6500 GL Nijmegen, The Netherlands
[12] Center for Astrophysics Harvard & Smithsonian: 60 Garden Street, Cambridge, MA 02138, USA
[13] NASA Goddard Space Flight Center, Astrophysics Division, Greenbelt, MD, 20771, USA
[14] STAR Institute, University of Liège, Quartier Agora - Bât. B5c Allée du Six Août 19C, 4000 Liège, Belgium
[15] Max-Planck-Institut für Radioastronomie, Auf dem Hügel 69, 53121 Bonn, Germany
[16] Institute of Theoretical Physics and Astrophysics, University of Kiel, Leibnizstraße 15, 24118 Kiel, Germany

Received 8 August 2025 / Accepted 2 February 2026

ABSTRACT

Context. Circumstellar discs, and especially their inner regions, which cover ranges from less than 1 au to a few au, are the birthplaces of terrestrial planets. The inner regions are thought to be as diverse in structure as the well-observed outer regions probed by ALMA.
Aims. By combining data and results from previous studies using the VLTI/PIONIER and VLTI/GRAVITY instruments with new, multi-epoch VLTI/MATISSE observations, we aim to provide a comprehensive picture of the structure of the inner regions of the circumstellar disc around the F-type Herbig Ae/Be star HD 142527 A, the primary of a binary star system.
Methods. We modelled the multi-wavelength interferometric data using a parametrised, geometrically thin disc model, allowing for azimuthal asymmetry, and exploring a first-order disc modulation and an off-centre Gaussian component.
Results. We find time-variable structures in the N-band observables, which we reproduce with time-dependent models. This variability manifests as azimuthally asymmetric emission, evidenced by strong, non-zero closure phases in the N-band data. Fits to individual epochs of the N-band observations yield better χ_r^2 values than fits to all epochs simultaneously. This suggests substantial changes in the geometry of the inner disc emission from ∼1 au up to a few astronomical-unit scales from one year to the next. Moreover, our models produce a very close-in inner disc rim $R_{\text{rim}} \approx 0.1$ au. Altogether, we find a very complex, substantially non-point symmetric and temporally variable disc ($r_{\text{out}} \lesssim 6$ au) around the primary.
Conclusions. The very close-in inner rim indicates the presence of material within the typical wall-like sublimation radius, $R_{\text{rim,literature}} \approx 0.3$ au. The complex, temporally variable inner-disc geometry is likely affected, or even caused by, the close passage (∼5 au) and short orbit ($P \approx 24$ yr) of the companion HD 142527 B.

Key words. techniques: interferometric – techniques: spectroscopic – protoplanetary disks – stars: individual: HD 142527 – stars: pre-main sequence – infrared: stars

1. Introduction

Herbig Ae/Be and T Tauri stars are often accompanied by planet-forming discs composed of gas and dust within the first 10 Myr of their existence. These discs are highly complex environments, with properties such as their mass and chemical composition influenced not only by the host star but also by various concurrent processes, including turbulence, winds, the dust grain growth and migration, and stellar accretion (Andrews et al. 2018; Andrews 2020; Benisty et al. 2023; Birnstiel 2024). Observations at millimetre wavelengths and scattered-light images at

---

[⋆] Corresponding author: `scheuck@mpia.de` optical and near-infrared (IR) wavelengths have mapped the outer regions of these discs (Pohl et al. 2017; Garufi et al. 2017, 2018), revealing diverse structures such as rings, radial gaps, spiral arms, dust clumps, and other azimuthal asymmetries (ALMA Partnership et al. 2015; Rubinstein et al. 2018). These regions also serve as a rich reservoir of gas and dust essential for planetary system formation, as supported by numerous studies examining various disc systems (e.g. Boccaletti et al. 2020). Recent research has also provided additional approaches to identify planets embedded within these discs (Fedele et al. 2017; Teague et al. 2018; Pinte et al. 2019), and in the case of PDS 70, at least two planets have been detected (Müller et al. 2018; Keppler et al. 2018; Haffert et al. 2019).

Similarly, the inner regions likely host smaller-scale structures akin to those observed in the outer disc (e.g. Menu et al. 2015; Varga et al. 2018; GRAVITY Collaboration 2021; Kluska et al. 2022; Varga et al. 2024; GRAVITY Collaboration 2024). Emerging evidence suggests that some of these substructures, such as radial gaps, arise from young, accreting planets (Haffert et al. 2019; Pinte et al. 2019).

We aim to expand knowledge of planet formation within circumstellar discs and to complement previous and concurrent research by studying the innermost regions of the discs (from <1 au scales up to a few au). Thus, we observed the mid-IR wavelength region with the spectro-interferometric Multi Aperture Mid-IR SpectroScopic Experiment (MATISSE) instrument (Lopez et al. 2022) located at the Very Large Telescopic Interferometer (VLTI) on Cerro Paranal in Chile and operated by the European Southern Observatory (ESO). The MATISSE instrument at the VLTI offers spatial resolutions superior to those of single telescopes (e.g. the James Webb Space Telescope) and provides a broad wavelength range. These resolutions facilitate the study of the structure of the innermost disc regions.

In this work, we focus on HD 142527, a binary system composed of an F-type Herbig Ae/Be star (Hunziker et al. 2021) accompanied by an M-dwarf companion (Biller et al. 2012; Lacour et al. 2016; Christiaens et al. 2018) on an eccentric orbit ($e \approx 0.45-0.7$, Claudi et al. 2019). HD 142527 A possesses a circumstellar disc, which was determined to be close to face-on by observations with the VLTI/Precision Integrated-Optics Near-infrared Imaging Experiment (PIONIER) (Lazareff et al. 2017) and VLTI/GRAVITY (GRAVITY Collaboration 2019) instruments and the Atacama Large Millimeter/submillimeter Array (ALMA) (Casassus et al. 2013). These observations showed inclination angles of $i_{\mathrm{in}} \approx 20-33^{\circ}$ and position angles of $\theta_{\mathrm{in}} \approx 5-20^{\circ}$ (east of north). For the inner disc, fits to the N-band emission indicate a radial gap within this region, which is not resolved by either the Spectro-Polarimetric High-Contrast Exoplanet Research (SPHERE) instrument or ALMA (Menu et al. 2015; Varga et al. 2018). The companion, HD 142527 B, lies close to the inner disc (periapsis to apoapsis: ~5 – 15 au) and orbits within a large gap in the surrounding circumbinary disc (~113 – 170 au from east to west) (Boehler et al. 2017). A possible explanation for the large gap between the inner and outer discs is one or more unseen planets (Lacour et al. 2016). From the shadows cast from the inner onto the outer disc, Marino et al. (2015) determined the misalignment ($\Delta\vartheta_{\text{in-out}} = 70^{\circ}$) and the position angle of the inner disc ($\theta_{\mathrm{in}} = (352 \pm 5)^{\circ}$). The inclination and position angle of the outer disc are estimated to be $i_{\mathrm{out}} = 38.^{\circ}21$ and $\theta_{\mathrm{out}} = 162.^{\circ}72$ from ALMA observations (Bohn et al. 2022). These, along with information on the stellar parameters of HD 142527 A and B, plus the parameters of the companion's orbit and the outer disc, are listed in Table 1.

In this work, we present MATISSE observations of HD 142527, combined with modelling of previous observations from PIONIER and GRAVITY data from Lazareff et al. (2017) and GRAVITY Collaboration (2019), respectively. Following earlier studies of young stellar objects (YSOs) (e.g. GRAVITY Collaboration 2021; Varga et al. 2024), we analyse these data using geometric disc models to determine the inner-disc structure. In contrast to these previous works, the extensive observations from the H to the N band also allow us to study the time variability of HD 142527 across different epochs.

The paper is structured as follows. In Sect. 2, we give an overview of the MATISSE observations and provide the necessary background on data reduction and quality assessment. We present first results, obtained directly from the observations, in Sect. 3. We explain our modelling approach in Sect. 4, and discuss it in Sect. 5, where we place the findings in a wider context. Finally, Sect. 6 summarises the main conclusions.

2. Observations

First, we provide a brief overview of the observations used, as well as the data treatment. Our work focuses on eight observations of HD 142527 on the MATISSE instrument taken from 2021 to 2023, as presented in Table A.1. These observations were obtained as part of the Guaranteed Time Observation (GTO) survey 'Initial conditions of planet formation in protoplanetary discs with GRA4MAT and MATISSE'. We excluded any observation with a coherence time $\tau_0 < 2$ ms, seeing $>1.5''$, or obvious artefacts (such as glitches during observations).

Each MATISSE dataset covers a wide wavelength range from the L/M (2.8 – 4.2 µm/4.5 – 5 µm) to the N band (8 – 13 µm). We obtained three of the eight datasets in the quadruplet using the 8.2 m Unit Telescopes (UTs). We obtained the remaining datasets with the 1.8 m Auxilliary Telescope (AT) in the small, medium, large, or extended configurations. With the associated baseline lengths $B \approx 10-130$ m, we reach spatial resolutions of $\theta = \frac{\lambda}{2B} \approx 30.9-2.4$ mas at 3 µm and $\theta \approx 123.8-9.5$ mas at 12 µm. We were able to combine the AT with the UT observations for HD 142527 because the inner disc is fully contained within the field of view (FOV) for all configurations, whereas the outer disc lies outside it, with any scattered light from it most likely resolved out. For the N band, we used only UT observations, as the ATs have a poor signal-to-noise ratio (S/N).

The bulk of the MATISSE data were reduced using a modification[1] to the 2.0.2 version of the MATISSE data reduction software (DRS)[2] (Millour et al. 2016) in combination with the MATISSE tools[3]. This modified version implements an improved coherent processing that uses the 2D Fourier transform of the interferograms (previously, it used the 1D Fourier transform), which provides more accurate estimates of the correlated flux and differential phase. To calibrate the data, we observed a bright, unresolved star with well-known properties (e.g. the limb-darkened diameter (LDD)) and time closely matching HD 142527. Varga et al. (2021) provide a detailed description of this calibration process.

From a standard reduction of a MATISSE observation, we obtain a total spectrum F_{ν} (averaged from the four individual VLTI telescopes), six correlated fluxes $F_{\nu,\mathrm{corr}}$, and four closure

---

[1] Expected to be included in the official 2.3.0 release by ESO.

[2] Provided by ESO at `https://www.eso.org/sci/software/pipelines/matisse`.

[3] Additional data-reduction tools are available at the MATISSE GitHub organisation: `https://github.com/Matisse-Consortium/tools`.

Table 1. Stellar parameters of HD 142527 A and B, together with outer disc and orbital parameters of the companion.

Parameter	Unit	Value	Reference
HD 142527			
RA (J2016)	(h:′:″)	15:56:41.87	(1)
Dec (J2016)	(°:′:″)	−42:19:23.67	(1)
d	(pc)	159.3 ± 0.7	(1)
HD 142527 A			
Spectral type		F2 – F3	(2^a)
$T_\star$	(K)	6500 ± 250	(2^a, 3, 4)
$M_\star$	($M_\odot$)	2.20 ± 0.05	(2^a)
$\log(L_\star/L_\odot)$		1.35 ± 0.01	(2^a)
$R_\star$	($R_\odot$)	3.46 ± 0.13	(2^a)
$t_\star$	(Myr)	$4.40^{+0.49}_{-0.38}$	(2^a)
HD 142527 B			
STAR			
Spectral type		$\mathrm{M}2.5 \pm 0.1$	(5)
$T_\star$	(K)	3500 ± 100	(5)
$M_\star$	($M_\odot$)	0.34 ± 0.06	(5)
$\log(L_\star/L_\odot)$		-0.60 ± 0.08	(5^b)
$R_\star$	($R_\odot$)	1.37 ± 0.05	(5)
$t_\star$	(Myr)	$1.8^{+1.2}_{-0.5}$	(5)
ORBIT			
a	(mas)	67.80 ± 1.38	(6^c)
e		0.47 ± 0.01	(6)
i	(°)	149.47 ± 0.71	(6)
ω	(°)	186.45 ± 0.48	(6)
Ω	(°)	161.51 ± 1.01	(6)
τ	(yr)	2020.42 ± 0.05	(6)
P	(yr)	23.50 ± 0.85	(6)
Outer disc			
$R_{\text{in, east}}$	(mas)	~ 714.29	(7^d)
$R_{\text{in, west}}$	(mas)	~ 1071.43	(7^d)
R_{out}	(mas)	~ 3500	(7^d)
$\Delta\vartheta_{\text{in-out}}$	(°)	70	(8)
i_{out}	(°)	38.21	(9)
θ_{out}	(°)	162.72	(9)

Notes. (1) Gaia Collaboration (2023); (2) Guzmán-Díaz et al. (2021); (3) Fairlamb et al. (2015); (4) Vioque et al. (2018); (5) Christiaens et al. (2018); (6) Nowak et al. (2024); (7) Fukagawa et al. (2006); (8) Marino et al. (2015). (9) Bohn et al. (2022). $^{(a,c,d)}$Converted to milliarsecond with *Gaia* EDR3 $d = 158.51$ pc (Gaia Collaboration 2021), *Gaia* DR3, and *Gaia* DR2 $d \approx 140$ pc distance (Gaia Collaboration 2018). $^{(b)}$Computed with $L = 4\pi R_\star^2 \sigma T_\star^4$ (Dullemond & Monnier 2010).

phases $\Phi_{\nu,\text{cp}}$. We produced the single-dish spectra from the incoherently reduced and chopped data, whereas the correlated fluxes and the closure phases stem from the coherently reduced, non-chopped data. The studies by Lopez et al. (2022) and Varga et al. (2021, 2024) provide detailed descriptions of a typical MATISSE observation and the data reduction. In this work, we provide a brief overview of the differences between the chopped and non-chopped observing modes, as well as the incoherent and coherent reduction methods. When chopping is active, the pointing of the telescopes intermittently switches from the object to the sky background. This improves the S/N of the total spectrum by enabling background subtraction, but interferes with the stability of the interferometric fringe tracking (Woillez et al. 2024). This worsens the quality of the correlated flux and differential phase measurements. We therefore used the non-chopping mode for these quantities. In this mode, the background for the interferometric observables is removed via optical path difference (OPD) modulation. During reduction in the coherent mode, the individual frames of the observation are aligned, preserving the phase information (Lopez et al. 2022). We then computed the noisy correlated flux estimator over the entire exposure, from which we extracted the correlated flux and the differential phase. In incoherent mode, we averaged the measured intensities without preserving the phase information of the individual frames (Petrov et al. 2020). We obtained all observations in this work either in low, medium, or high spectral resolution and then binned them to low resolution during the reduction and post-processing. This yielded data with spectral resolutions of $R = \frac{\lambda}{\Delta\lambda} \approx 34$ in the L and M band, and of $R \approx 30$ in the N band.

In addition to the MATISSE data, we used archival H band (1.5 – 1.85 µm) observations from the Optical interferometry DataBase (OiDB) at the Jean-Marie Mariotti Centre (JMMC), obtained with the PIONIER instrument (Lazareff et al. 2017). Moreover, we used K band observations (1.95 – 2.45 µm) provided by the GRAVITY collaboration (GRAVITY Collaboration 2017).

3. Results

Before modelling, we interpret the calibrated data from the Figs. presented in Appendix A. Within the H, K, L, and N bands, the correlated fluxes reach values of 3.46, 3.02, 2.03, and 0.63 Jy for the longest baselines of 139.93, 129.23, 130.19, and 130.19 m, across all observations. For the same observations and baselines, the closure phases reach values of $2.^\circ67$, $2.^\circ52$, $10.^\circ97$, and $47.^\circ20$.

We focus on the N-band data of HD 142527 as they allow us to probe the disc up to a few astronomical units. The correlated fluxes reveal contributions from spatially unresolved disc regions. At first order, longer baselines (i.e. higher spatial frequencies), probe disc regions closer to the centre and smaller in extent (Buscher 2015). The lower spatial frequencies of the N band, coupled with its sensitivity to cooler dust, make it a good indicator of the structure and composition of the extended inner disc regions (up to ∼10 au). Moreover, HD 142527 shows strong silicate features in both total spectra and correlated fluxes (Fig. A.1). In particular, in the N band, the silicate features disappear at several spatial frequencies (Figs. A.4 and A.5). This could indicate a multiple-zone structure that cancels the silicate emission (e.g. Varga et al. 2024). The prominence of the silicate feature aligns with previous observations by van Boekel et al. (2005) and Juhász et al. (2010). The total spectra of the three epochs exhibit a very similar shape, with several crystalline silicate peaks, notably the 11.3 µm forsterite peak. Moreover, we find a ∼10 % flux-level variability across the epochs. This variation remains within the flux calibration uncertainties and is consistent with archival N-band data obtained with Wide-field Infrared Survey Explorer (WISE), Infrared Space Observatory (ISO)/Short Wavelength Spectrometer (SWS), and Spitzer Space Telescope (SPITZER). The other N-band observable is the closure phase $\Phi_{\nu,\text{cp}}$, which traces brightness asymmetries. HD 142527 shows large closure phases across epochs, suggesting a complex structure.

In contrast, the shorter-wavelength bands (H, K, L, and M) resolve compact structure close to the star (sub-au scales), due to the higher spatial frequencies from the AT observation. This wavelength range shows a less pronounced signal for the closure phase, which increases from the H band to the M band.

Comparing the N-band observations to the shorter wavelengths reveals that HD 142527 is already quite resolved (i.e. the correlated fluxes are closer to zero), whereas the opposite holds for the shorter wavelengths. This results partly from the star contributing more at the shorter wavelengths, yielding higher correlated fluxes. Moreover, we observe a first zero-crossing of the complex correlated fluxes at spatial frequencies $\sim 15\,\mathrm{M}\lambda$, with the next zero-crossing presumably occurring at spatial frequencies beyond our coverage ($\sim 120-150\,\mathrm{M}\lambda$). The spatial frequency of zero-crossings is a particularly robust feature of our data, as it is unaffected by calibration uncertainties. An increase in the closure phase from the H to the N band is also apparent. This indicates a relatively symmetric structure on the smallest scales we resolve, whereas the larger scales of $\sim$1 au show stronger asymmetry. This asymmetry suggests a two-component structure with an asymmetric, extended component at longer wavelengths and a more compact, relatively symmetric component at shorter wavelengths. We explore this further through geometric modelling in Sects. 4.3 and 5.

4. Modelling

We model our data using a geometrically thin disc model, first without and then with azimuthal asymmetries. We obtain the opacity of the disc material from a fit to the total spectrum in the N band (Sect. 4.1), which reveals a silicate emission feature with strong signs of high-temperature dust processing (e.g. Bouwman et al. 2001; van Boekel et al. 2004, 2005; Juhász et al. 2010). From this fit, we derive a ‘silicate’ and ‘continuum’ opacity component that we use in the interferometric modelling, allowing their relative ratio to vary across the different disc zones (Section 4.2.2).

As we lack sufficient sampling of spatial frequencies (u, v) for image reconstruction, we applied a parametric modelling approach. We fitted our model M to data $\boldsymbol{D}$ using Bayesian inference, implemented via the `dynesty` package (Speagle 2020). The stopping criterion for this algorithm is the difference $\Delta \ln \mathcal{Z}_i$ between the current estimated $\mathcal{Z}_i$ and the remaining evidence $\Delta\mathcal{Z}_i$ at each iteration i. We chose $\Delta \ln \mathcal{Z}_i < 0.01$, which ensures convergence when the sampler terminates. We employed flat priors $\pi(\boldsymbol{\Theta}) \equiv P(\boldsymbol{\Theta}, M)$ for all parameters. The number of live points K_i (i.e. samples drawn from the prior volume X) was set to 1000. Parameter values $\boldsymbol{\Theta}$ are the sample median, while the lower and upper uncertainties are the samples at 2.5 and 97.5%, respectively. Appendix B provides further details on the fitting algorithm and Table C.1 gives an overview of all model parameters.

We de-reddened the data, assuming foreground extinction (see Appendix D.1) to enable the comparison of the model to the data. To ensure an equal weighting of the wavelength bands during the model fitting, we imposed a lower limit on the errors: a minimum of 5% (of the data) for the total spectrum and correlated fluxes, and 5° for the closure phases. For computational efficiency, we applied spectral binning with a window size of $\Delta\lambda = 0.2\,\mu\mathrm{m}$ for the H and K bands, and $\Delta\lambda = 0.1\,\mu\mathrm{m}$ for the remaining bands.

4.1. Dust opacity model

We determined the opacity of disc material around HD 142527 A from a fit to the total N-band spectrum. This was not a quantitative dust-spectroscopy analysis; rather, we sought a well-fitting opacity across the disc model’s wavelength range (Sect. 4.2.2).

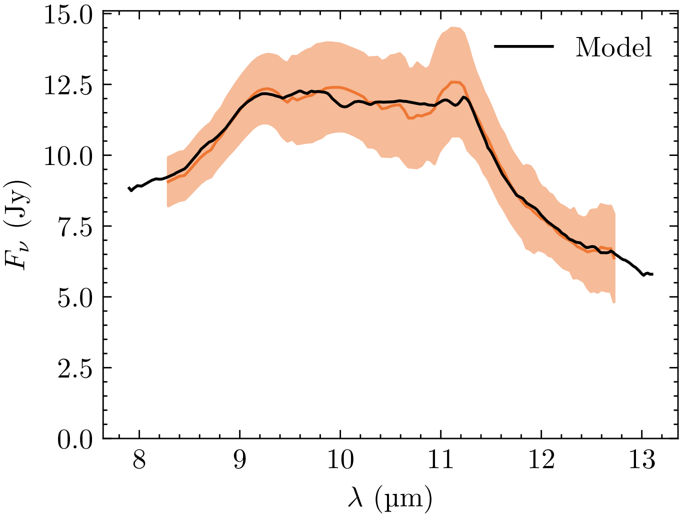

Fig. 1. Opacity fit. The model (black) overlays the averaged N-band UT data (orange). We exclude the PAH flux contribution from the model curve, as in the disc modelling in Sect. 4.2.

The dust opacity model (see van Boekel et al. 2005) is described in Appendix E. Table E.1 and Fig. 1 present the resulting best-fit dust composition[4].

The HD 142527 system is unresolved in the total spectrum and thus does not provide insight into the disc’s dust composition or its local distribution. In contrast, the correlated fluxes provide spatial information on the dust composition (e.g. Varga et al. 2024). Nevertheless, for simplicity, we kept the silicate mineralogy spatially constant in our modelling, allowing only changes to the silicate-to-carbonaceous ratio (Eq. (4)). Consequently, our disc models do not reproduce the mineralogy gradient of the correlated fluxes (Fig. A.4).

4.2. Model components

Our disc models consist of a central star (i.e. a point source; Sect. 4.2.1), an asymmetric temperature-gradient disc (Sect. 4.2.2), and an off-centre Gaussian component (Sect. 4.2.3). We derive the complex correlated fluxes $\mathfrak{F}_\nu(q')$[5] below. Appendix F shows the computation of the observables from the complex correlated flux, and an in-depth description of all applied models follows in Sect. 4.3.

4.2.1. Star

The primary star is the central component of the disc model. Its estimated angular diameter is only ≈0.23 mas (see Appendix D), so the star remains spatially unresolved in our observations. We treat it as a point source, whose complex correlated flux is given by

$$\mathfrak{F}_{\nu,\star} = F_{\nu,\star} \exp(2\pi i q'(\alpha\cos(\psi) + \beta\sin(\psi))), \quad (1)$$

where α and β are the angular coordinates (in radians) of the image plane in directions of right ascension (RA), and (Dec), respectively, and ψ is the angle corresponding to the de-projected

---

[4] Detailed analysis from van Boekel et al. (2005) and/or Juhász et al. (2010) (both using grains computed via the DHS method) yield dust compositions significantly different from ours.

[5] For brevity, we shorten the de-projected spatial frequency $q' = q'(i, \theta)$ and omit it as a parameter of the complex correlated flux.

spatial frequency q'. For the fitting procedure, we used the polar representation of the angular coordinates, where ρ is the separation from the centre and the position angle Φ (east of north) (Berger & Segransan 2007). Appendix D.1 details the derivation of the stellar flux $F_{\nu,\star}$.

4.2.2. Asymmetric temperature-gradient disc

The disc model consists of one or more zones surrounding the primary star. Each zone (index n) is the result of integrating over infinitesimally thin rings (see Berger & Segransan 2007) with an emergent intensity $I_{\nu,n}$. These rings can include an additional azimuthal modulation (Lazareff et al. 2017). We now describe the emergent intensity using a power-law approach and show how it connects to the complex correlated flux.

We require the source function $B_\nu(T)$ to determine the zone intensity. The source function depends on a temperature distribution:

$$T(r) = T_0 \left(\frac{r}{R_0}\right)^q. \tag{2}$$

The radial behaviour of the temperature profile is determined by its power-law index q, where T_0 is the temperature at reference radius $R_0 = 1$ au. Multiple zones share a single temperature profile. We also need the emissivity $\epsilon_{\nu,n}$ to describe the intensity. The emissivity depends on the optical depth $\tau_{\nu,n}$, itself determined by the zone surface density:

$$\Sigma_n(r) = \Sigma_{0,n} \left(\frac{r}{R_0}\right)^{p_n}. \tag{3}$$

Here, $\Sigma_{0,n}$ is the surface density at R_0 and p_n is the power-law index. Combined with the absorption-opacity curve of silicates $\kappa_{\nu,\mathrm{abs,sil}}$, the carbonaceous grain continuum $\kappa_{\nu,\mathrm{abs,cont}}$, and the mass fraction $w_{\mathrm{cont},n}$, we obtain the vertical optical depth

$$\tau_{\nu,n}(r) = \Sigma_n(r)[(1 - w_{\mathrm{cont},n})\kappa_{\nu,\mathrm{abs,sil}} + w_{\mathrm{cont},n}\kappa_{\nu,\mathrm{abs,cont}}]. \tag{4}$$

Accounting for inclination effects, the vertical optical depth is modified along the line of sight, and we obtain the emissivity

$$\epsilon_{\nu,n}(r) = 1 - e^{-\tau_{\nu,n}(r)/\cos(i)}. \tag{5}$$

Multiplying this emissivity by the radially dependent source function gives the emergent intensity of the zone:

$$I_{\nu,n}(r) = \epsilon_{\nu,n}(r) B_\nu\left(T(r)\right). \tag{6}$$

From Lazareff et al. (2017) we obtain the complex correlated flux for an azimuthally modulated, infinitesimally thin ring:

$$\mathfrak{F}_{\nu,\mathrm{ring},n} = \sum_{m=0}^{\ell} (-\mathrm{i})^m A_{n,m} \cos(m(\psi - \phi_{n,m})) J_m\left(\frac{2\pi q'\nu}{c} r\right). \tag{7}$$

Here, J_m is the Bessel function of the first kind of order m, $A_{n,m}$ is the modulation amplitude, and $\phi_{n,m}$ is the modulation angle. All orders up to ℓ contribute to the ring, which is symmetric for $\ell = 0$ (i.e. J_0 and $A_{n,0} = 1$), and azimuthally asymmetric for $\ell \geq 1$. Using the intensity of Eq. (6) and integrating over the solid angle Ω yields the complex correlated flux for the azimuthally modulated disc zone,

$$\mathfrak{F}_{\nu,n} = 2\pi \cos(i) \int_{R_{\mathrm{in},n}}^{R_{\mathrm{out},n}} \mathfrak{F}_{\nu,\mathrm{ring},n} I_{\nu,n}(r) r \,\mathrm{d}r. \tag{8}$$

The zone extends from an inner radius $R_{\mathrm{in},n}$ to an outer radius $R_{\mathrm{out},n}$. For this component, we used the ALMA observations of the outer disc from Bohn et al. (2022) in combination with the misalignment ($\Delta\vartheta_{\text{in-out}} = 70°$) from Marino et al. (2015) (see also Table 1) to compute[6] the inclination of the inner disc, and fix the inclination to $i_{\mathrm{in}} = 32\overset{\circ}{.}05$ and the position angle to $\theta_{\mathrm{in}} = 352°$. We followed this approach because Nowak et al. (2024) demonstrate that the angle convention of Bohn et al. (2022) is inconsistent with the observed shadows cast by the inner disc onto the outer disc of HD 142527.

4.2.3. Gaussian

The correlated-flux behaviour (i.e. the zero-crossing; see Sect. 3) suggests a more spatially confined asymmetric component. We therefore chose an off-centre Gaussian whose complex correlated flux (given by Berger & Segransan 2007) we multiply by a source function $B_\nu(T(\rho))$, a scale factor f, and the emissivity ϵ_ν as follows:

$$\mathfrak{F}_{\nu,\mathrm{Gauss}} = f \epsilon_\nu B_\nu(T(\rho)) \exp\left(-\frac{(\pi a q')^2}{4 \ln 2}\right). \tag{9}$$

Here, the temperature is computed via Eq. (2), using the power law of the accompanying disc component(s) $T(r)$ at Gaussian position ρ. The Gaussian size is given by the full width at half maximum (FWHM) a. The emissivity follows Eq. (5), except that Σ is a fit parameter rather than a power-law derivation.

As we cannot resolve this component and assume that it is compact, we fixed the FWHM to $a = 2.57$ mas ($\approx$0.41 au for $d = 159.3$ pc). This choice provides sufficient flux to reproduce the signatures seen in the data while keeping the component unresolved in the N band.

4.3. Model geometries

The following section describes the modelling approaches used in this work. Each model is centred on a point source (Sect. 4.2.1) representing HD 142527 A. We excluded the companion HD 142527 B from our model because it is 4.5 mag fainter than the primary in the H band (see Lacour et al. 2016) and shows no definite signal in our data.

Previous studies indicate a gapped disc around HD 142527 A (e.g. Menu et al. 2015). We therefore first compared two azimuthally symmetric disc models (Sect. 4.2.2): a one-zone (continuous) and a two-zone (gapped) disc model. Using this symmetric approach, the gapped model provided the best fit to the data.

To reproduce the large closure phases in the N band (Sect. 3), we introduced an asymmetry. We selected the simplest asymmetric model; a first-order azimuthal modulation ($\ell = 1$). Using this asymmetric two-zone disc model, we observe three effects. First, the large errors on the closure phases of the H, K, and L bands prevented us from constraining the modulation of the inner zone, although the formal goodness of fit improved. Furthermore, the closure phases of these bands exhibit only a weak signal. This wavelength region is dominated by the innermost disc. To reduce the number of free parameters, we removed the modulation of the inner zone and retrained only the outer zone modulation. Second, a global asymmetry failed to adequately reproduce all visibility and phase signals, particularly the zero-point crossing,

---

[6] For this computation, we rearranged and recursively solved Eq. (7) from Bohn et al. (2022): $i_{\mathrm{in}} = \arccos[(\cos(\Delta\vartheta_{\text{in-out}}) - \sin(i_{\mathrm{in}})\sin(i_{\mathrm{out}})\cos(\theta_{\mathrm{in}} - \theta_{\mathrm{out}}))/\cos(i_{\mathrm{out}})]$.

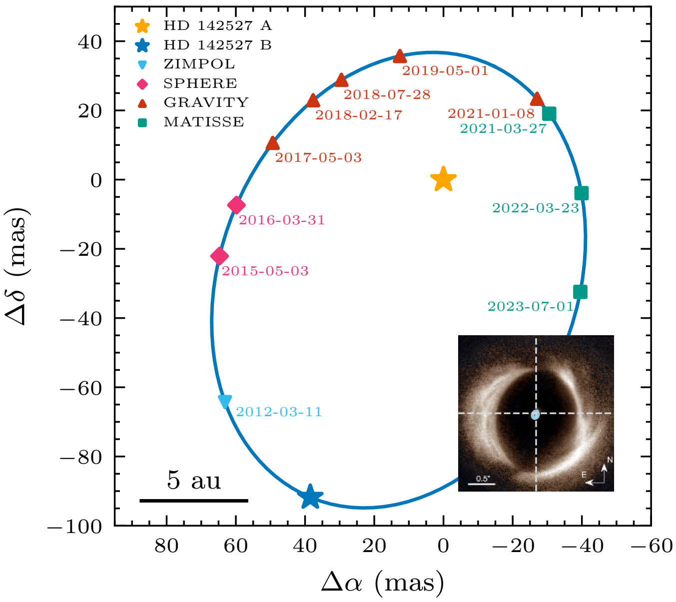

Fig. 2. System sketch. The host star HD 142527 A (orange star) is orbited by its companion HD 142527 B (blue star at apoapsis). We computed the orbit (blue) using parameters from Nowak et al. (2024) and used the same parameters to derive the positions of the MATISSE epochs (teal squares). *Bottom right*: SPHERE observations of the outer disc (Avenhaus et al. 2017) showing the orbit (light blue) of the companion.

which is the most robust feature of our dataset (see Fig. A.4) and is unaffected by systematics or calibration issues. We infer that fitting this feature requires a more localised, smaller asymmetric emission than the global $\ell = 1$ modulation. Third, fitting all N-band data simultaneously results in a worse $\chi^2_{\rm r}$ than fitting the individual N-band epochs with epoch-dependent parameters. This suggests temporal variability in the N-band intensity distribution.

We therefore tested simple localised asymmetric emission, specifically an off-centre Gaussian. This phenomenological modelling approach yields significantly better fits than the first-order modulation. Epochs-specific fits again yield better results than fitting one model to all epochs simultaneously. This supports the assumed temporal variability, which we interpret in Sect. 5.2.

Due to the limited (u, v) coverage per epoch and the evidence for temporal variability, we did not attempt to fit more complex model geometries.

5. Discussion

5.1. The role of the stellar companion

We calculated the orbit of the companion HD 142527 B using the parameters of Nowak et al. (2024) listed in Table 1 and find that the three N-band UT observations occurred near periapsis passage (Fig. 2). We suggest that this close passage, combined with the short orbital period (~24 yr), strongly perturbs the disc, creating a complex and time-variable disc structure.

To infer the companion's influence on the primary's disc, we compute the Hill radius (Eggleton 1983; Hamilton & Burns 1992):

$$R_{\rm H} \approx a(1-e)\sqrt[3]{\frac{M_{\rm B}}{3(M_{\rm A}+M_{\rm B})}}. \tag{10}$$

Table 2. Comparison of fit goodness (i.e. $\chi^2_{\rm r,tot}$) per model.

	M1	M2	M3
All epochs	10.54	8.26	4.47
Epoch 1	10.54	5.50	2.44
Epoch 2	10.54	7.30	1.89
Epoch 3	10.54	3.07	1.64

Notes. For the calculation of these values, see Appendix B. *First row*: time-invariant models fit to all data simultaneously. *Second to last row*: the same models with additional free parameters per N-band epoch. 'M1': symmetric (time-invariant) two-zone disc model; 'M2': M1 with an asymmetry in the outer zone; 'M3': one-zone disc model with an off-centre Gaussian asymmetry.

Here, a is the semi-major axis, e is the eccentricity, and $M_{\rm A}$ and $M_{\rm B}$ are the masses of the primary and secondary, respectively. Applying the stellar parameters from Table 1, Eq. (10) results in $R_{\rm H} \approx 2$ au, roughly half the separation between the primary and secondary (~5 au). This strongly influences the disc ($r_{\rm out} \lesssim 6$ au) and likely generates complex structures. Moreover, perturbations caused by interactions with the secondary may deplete disc material, necessitating replenishment processes to explain the continued existence of the disc (e.g. streamers, see Casassus et al. 2015).

The companion could also induce a time-variable asymmetry through alternative mechanisms, such as heating the disc midplane or via shock processes. This would also explain the high crystallinity observed in HD 142527 by providing temperatures sufficient to crystallise additional dust farther from the primary (Harker & Desch 2002; van Boekel et al. 2004). The SPHERE observations by Avenhaus et al. (2017) support this scenario, revealing complex emissions just beyond 4 au.

5.2. Nature of the asymmetry

To investigate the prominent N-band asymmetry, we build on the step-by-step evolution of our modelling approaches described in Sect. 4.3 and demonstrate that time-variable models, which account for the possibility of interactions between the disc and companion (Sect. 5.1), yield the best results. Table 2 compares the goodness-of-fit of the different model geometries.

Fully symmetric models (e.g. M1) cannot reproduce the non-zero closure phases observed in the N band. We first confirmed that a gapped disc (i.e. two-zone disc) model could be a good fit to the data. This is supported by the disappearance of the silicate feature in the correlated fluxes at some spatial frequencies (Figs. A.1 and A.4) similar to HD 144432, where a secondary component counteracted the silicate emission from the primary component (Varga et al. 2024). In the asymmetric two-zone model, further evidence for a gap comes from the resolved component in the N-band correlated fluxes and the decreasing closure phases at shorter wavelengths (Sect. 3), which indicates a less asymmetric structure closer to the star.

However, in Sect. 4.3, we note that the zero-crossing, a robust feature of our data, is not reproduced by the time-variable two-zone disc model, while the first and third epochs (2021 and 2023) are reasonably well-fitted. This suggests that the true intensity distribution on-sky exhibits a more spatially confined, off-axis emission component than a disc with a global cosine-like azimuthal intensity modulation can provide.

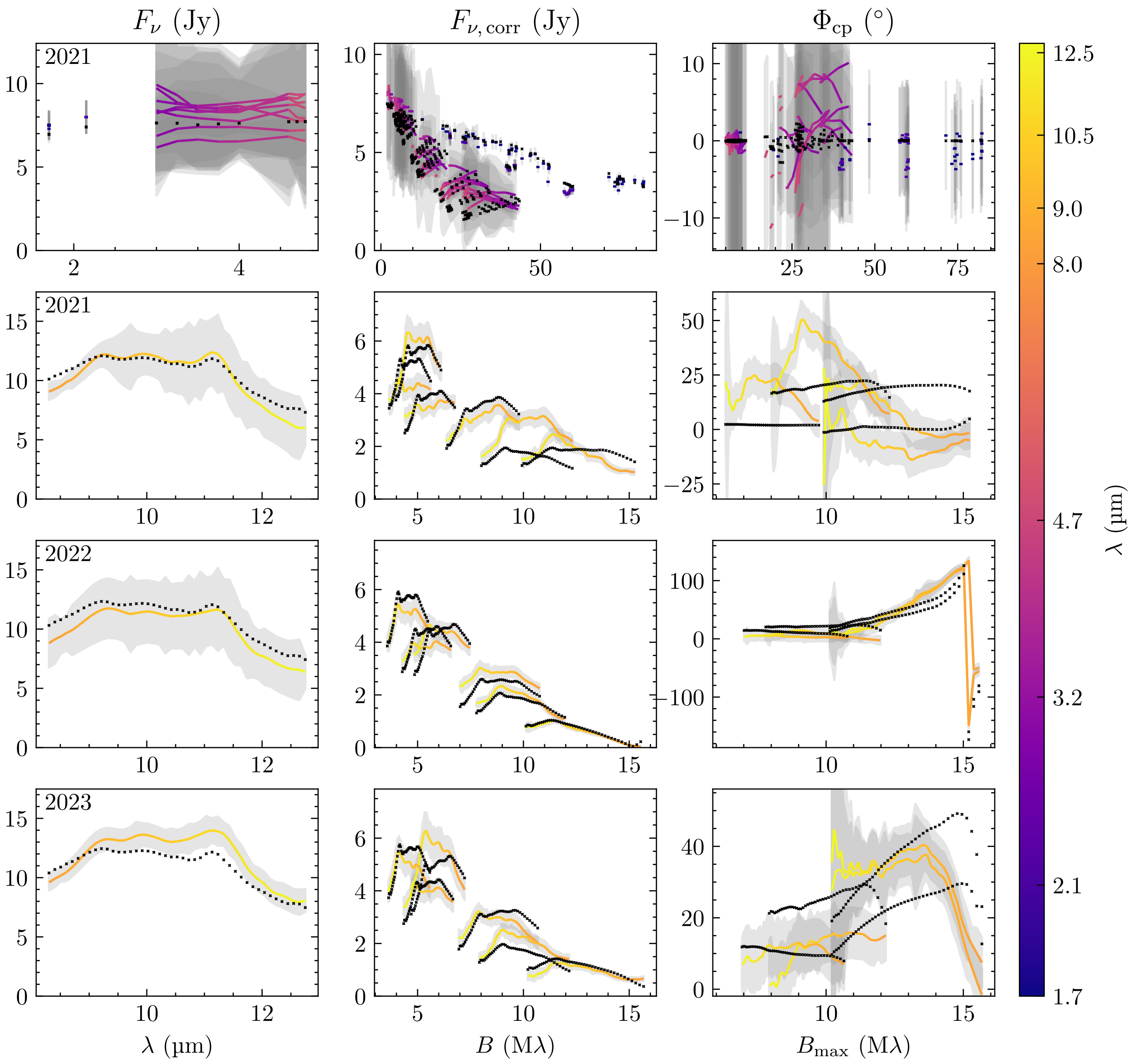

Fig. 3. Best-fit, one-zone disc model with off-centre Gaussian asymmetry. The data (coloured lines) are overlaid with the model (black crosses). Figure G.1 shows the residuals of the plots. *Left*: total spectrum F_ν. *Middle*: correlated fluxes $F_{\nu,\mathrm{corr}}$. *Right*: closure phases $\Phi_{\nu,\mathrm{cp}}$. *Top*: PIONIER (*H* band), GRAVITY (*K* band), and MATISSE (*L* and *M* band) data, fitted with all *N*-band datasets. *Row 1*: fit to the shorter wavelengths shown at the example of the first *N*-band epoch. *Rows 2–4*: first to third *N*-band epochs (2021, 2022, and 2023).

We therefore constructed a model with a central star, an azimuthally symmetric disc component, and a relatively compact off-axis component. We assume that the off-axis component is too compact to be significantly spatially resolved in the *N* band and, for simplicity, model it as a symmetric Gaussian with a FWHM of $a \approx 2.6$ mas. The free parameters in this model are the Gaussian's position relative to the disc centre for each epoch and its relative intensity across all epochs. This approach successfully reproduces the zero-crossing in the 2022 epoch. Figs. 3 and 4 illustrate this model, while Table 3 lists the best-fit parameters.

We tested whether the angular position of the asymmetry correlates with the companion's position[7], but find no clear correlation between the companion and the best-fit position of the asymmetry per epoch. Neither of the explored models fully reproduces the observations, and in both cases the asymmetric element changes substantially from one epoch to the next, even between the second and third epochs, where the difference in the hour angle of the observations, and hence (u, v) coverage, is small. This suggests that the true intensity distribution is more complex than the models explored here and varies on the ~1 yr timescale that our observations probe.

Given the limited (u, v) coverage of a single observation, fitting a model with significantly more complexity than the geometries explored here is not justified. At the same time, temporal variability complicates the combination of observations obtained over several years. Objects such as HD 142527 require dedicated imaging-like campaigns with the UTs, in which good (u, v) coverage is collected within a time span $\ll$1 yr.

---

[7] $\theta_\mathrm{B} = 301\overset{\circ}{.}882, 264\overset{\circ}{.}368, 230\overset{\circ}{.}611$ east of north, for epochs 2021, 2022, and 2023, respectively.

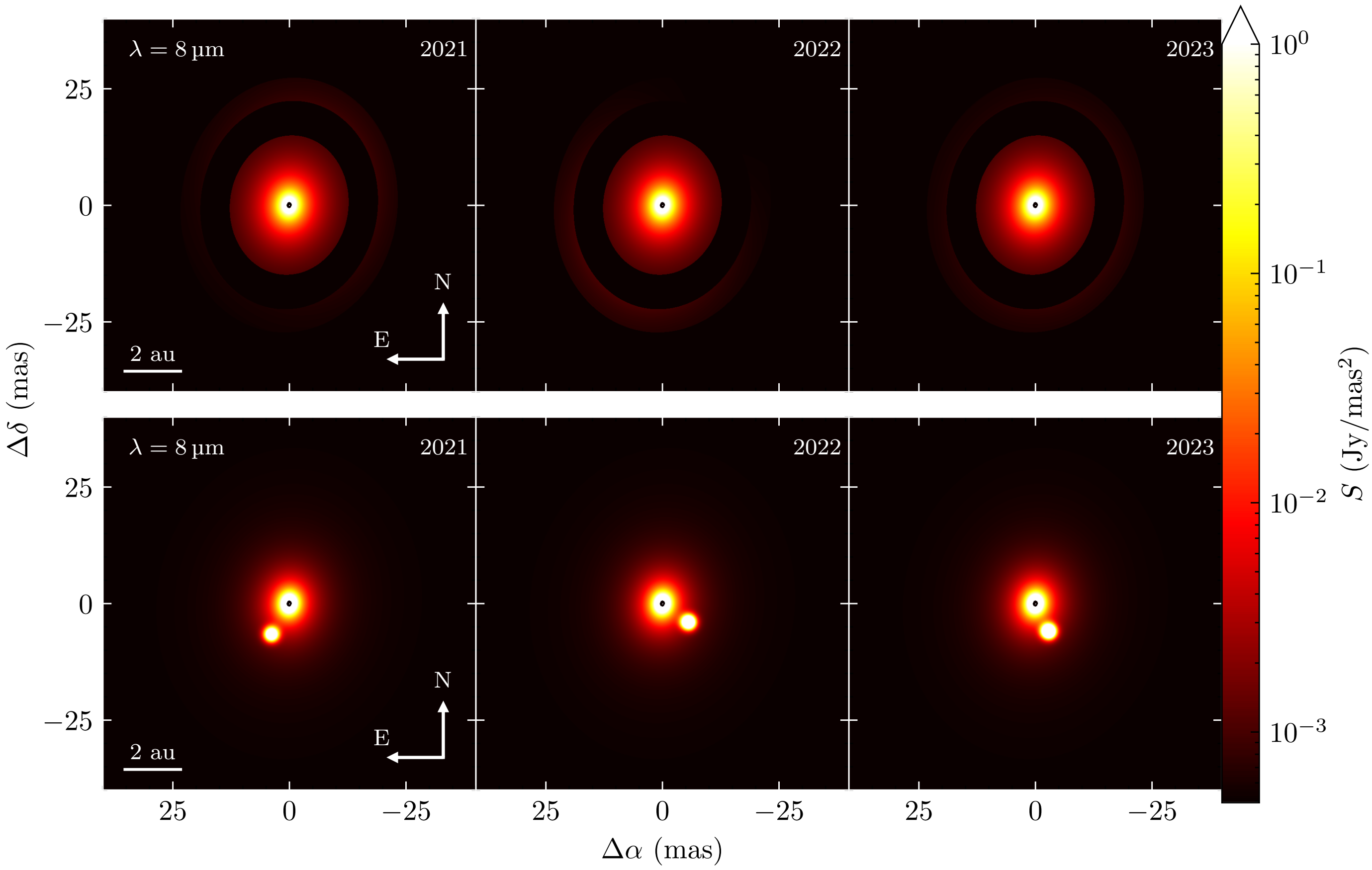

Fig. 4. Model surface-brightness images. *Left to right*: Epochs 2021, 2022, and 2023. *Top*: two-zone disc model. *Bottom*: best-fit, one-zone disc model with a Gaussian.

Nevertheless, our qualitative findings (i.e. a geometry deviating strongly from an azimuthally symmetric configuration with temporal variability on $\lesssim$1 yr timescales) provide useful insight into the gravitational interaction between the circumprimary disc and the low-mass stellar companion on its highly eccentric orbit. Price et al. (2018) presents simulations of this system[8] in which the inner disc is strongly distorted during each periapsis passage of the companion and does not have time to settle between periastron passages. The disturbance proceeds from the outside-in, such that disc regions of roughly 1-few au, to which our N-band observations are sensitive, are more strongly affected than the regions closer to the star probed by our L-band observations. In the L band, we see a more symmetric, less distorted geometry, as indicated by the smaller closure phases compared to the N band. The orbital parameters of the HD 142527 system have been substantially revised since Price et al. (2018) with the orbit derived by Nowak et al. (2024), having both a shorter period and a closer periapsis distance than any of the configurations explored in the earlier simulations. A strongly distorted and temporally variable geometry is therefore likely, and we conclude that our observations qualitatively support this scenario, but emphasise the need for a dedicated interferometric imaging-like observation strategy with the UTs.

5.3. A very close-in rim

Throughout the different model geometries, we consistently find the innder disc rim at $R_\mathrm{rim} \approx 0.1$ au. Assuming a sublimation temperature of $T_\mathrm{rim,literature} = 1500$ K and inserting this, together with the values from Table 1, into the expression for the sublimation radius (Dullemond & Monnier 2010),

$$R_\mathrm{rim} = \sqrt{\frac{L_\star}{4\pi\sigma T_\mathrm{rim}^4}} = R_\star \left(\frac{T_\star}{T_\mathrm{rim}}\right)^2, \tag{11}$$

results in $R_\mathrm{rim} = 0.3$ au. Here, T_rim is the temperature at the inner rim of the disc, σ is the Stefan-Boltzmann constant, and $L_\star$, $R_\star$, and $T_\star$ are the stellar luminosity, radius, and effective temperature, respectively. The sublimation radius computed from the theoretical assumption does not agree with the value derived from our data. However, such a close-in inner rim is supported by previous studies (e.g. Benisty et al. 2010b, 2011; Varga et al. 2024). These studies reported material located beyond the sublimation radius and/or at temperatures higher than expected. In addition, earlier studies on this target by the PIONIER (Lazareff et al. 2017) survey determined $R_\mathrm{rim} \approx 0.05$ au, and $R_\mathrm{rim} \approx 0.13$ au with the GRAVITY (GRAVITY Collaboration 2019) survey. We compare the theoretically assumed temperature at the inner rim by computing the temperature at $R_\mathrm{rim} = 0.1$ au with the power law of our best-fit model ($T_0 = 599.74$ K and $q = -0.55$; Table 3). This yields a sublimation temperature $T_\mathrm{rim} \approx 2100$ K that differs by ~600 K from literature values. Several factors may contribute to this discrepancy between the calculation and the model fit. First, the assumed sublimation temperature $T_\mathrm{rim,literature} = 1500$ K, is an oversimplification, as it does not account for the diversity of dust grains (Gail 2004). Various materials sublimate at higher temperatures.

---

[8] Available at `https://users.monash.edu.au/~dprice/pubs/HD142527/`.

Table 3. Parameters of the best-fit, time-dependent, one-zone disc model with a Gaussian asymmetry (corresponding to model M3 in Table 2).

Parameter	Unit	Value
FREE		
$R_{\text{out, 1}}$	(au)	$5.32^{+0.07}_{-0.06}$
$w_{\text{cont, 1}}$	(%)	$79.30^{+0.98}_{-0.87}$
$\Sigma_{0,1}$	$(10^{-4}\,\text{g cm}^{-2})$	$1.24^{+0.03}_{-0.02}$
p_1		0.29 ± 0.01
$\log(f/\text{sr})$		15.30 ± 0.01
$\rho_{\text{Gauss, t0}}$	(au)	1.21 ± 0.03
$\rho_{\text{Gauss, t1}}$	(au)	1.10 ± 0.01
$\rho_{\text{Gauss, t2}}$	(au)	$1.06^{+0.02}_{-0.01}$
$\Phi_{\text{Gauss, t0}}$	(°)	$150.11^{+2.02}_{-1.97}$
$\Phi_{\text{Gauss, t1}}$	(°)	$-125.34^{+1.49}_{-1.09}$
$\Phi_{\text{Gauss, t2}}$	(°)	$-154.24^{+1.62}_{-2.00}$
Σ_{Gauss}	$(10^{-4}\,\text{g cm}^{-2})$	$16.90^{+0.56}_{-0.68}$
$w_{\text{cont, Gauss}}$	(%)	$60.71^{+36.86}_{-58.19}$
T_0	(K)	$599.74^{+2.61}_{-3.11}$
FIXED		
$R_{\text{in},1}$	(au)	0.1
q		−0.55
d	(pc)	159.3
i_{in}	(°)	32.05
θ_{in}	(°)	352
a	(au)	0.41
χ^2_{r,F_ν}		4.13
$\chi^2_{r,F_{\nu,\text{corr}}}$		3.00
$\chi^2_{r,\Phi_{\nu,\text{cp}}}$		3.86
$\chi^2_{\text{r, tot}}$		3.36

Notes. For each parameter, the value is the median of the samples, with the uncertainties being the samples at 2.5 and 97.5%. The index t indicates a time-variability ('t0': epoch 2021, 't1': epoch 2021, and 't2': epoch 2023). All angles are given in the east of north direction.

Varga et al. (2024) and Flock et al. (2025) present different materials that could explain a close-in inner rim. Examples include corundum ($T_{\text{rim}} \approx 1850$ K) and tungsten ($T_{\text{rim}} \approx 2000$ K). However, chemical equilibrium modelling by Varga et al. (2024) predicts that these species occur at abundances too low to produce observable spectral features, which are indeed absent. In our modelling, we therefore chose amorphous carbonaceous grains for the continuum as these are featureless across our wavelengths. Iron grains would perform better than carbonaceous grains (see Appendix E). Their presence in the inner regions is supported by observations of atomic jets containing iron (Assani et al. 2024; Caratti o Garatti et al. 2024), which require high speeds only available closer to the star. However, because iron is also featureless, we cannot distinguish it from carbonaceous grains in our modelling. Another potential explanation for the very close-in inner rim is emission from hot gases. Benisty et al. (2010a) showed that emission from hot gas in these regions, would require the presence of spectral lines in the spectral energy distribution (SED). We therefore inspected archival X-shooter spectra of HD 142527 (Mendigutía et al. 2014; Fairlamb et al. 2015) for emission lines in the near infrared. These spectra show hydrogen lines (Br$_\gamma$, Pa$_{\beta,\gamma}$) and a few weak, isolated lines that we did not identify. This is inconsistent with dense gas being the dominant source of opacity in the inner disc region. We therefore conclude that dust likely survives farther inward and is detected by our observations (e.g. Klarmann et al. 2017).

6. Summary and conclusions

We present a chromatic and geometric disc model (Sect. 4) to probe the composition and structure of the circumstellar disc around HD 142527 A. We used photometric and interferometric data in the infrared spanning a wide wavelength range, from archival VLTI/PIONIER observations (H band) to VLTI/GRAVITY data (K band), and new observations from our GTO VLTI/MATISSE survey (L, M, and N bands).

Our key findings can be summarised as follows.

1. Our MATISSE data reveal large closure phases $\Phi_{\nu,\text{cp}}$ and strong silicate features in both total spectra F_ν and correlated fluxes $F_{\nu,\text{corr}}$ (Sect. 3), confirming earlier observations by van Boekel et al. (2005) and Juhász et al. (2010). The closure phase signals increase in amplitude with wavelength, while the silicate features weaken towards longer baselines and vanish entirely at some spatial frequencies.
2. Both models we applied, a two-zone disc (Sect. 4.2.2) with a first-order modulation in the outer zone and a one-zone disc with a localised off-centre Gaussian asymmetry (Sect. 4.2.3), fail reproduce the N band of all epochs simultaneously. Only the best-fit model incorporating an off-centre Gaussian reproduces the robust zero-crossing measurement observed in the 2022 epoch (Fig. 3).
3. We obtain the best fit to our data by implementing a time-dependent asymmetry for each N-band epoch and incorporating information from the shorter wavelength bands. To achieve this, the parameters defining the asymmetry have an iteration for each epoch, while the remaining parameters are shared across epochs (Sect. 5.1).
4. By combining the near-IR with the new L-band information, we place the inner rim at $R_{\text{rim}} \approx 0.1$ au (Sect. 5.3). This is consistent with earlier H- and K-band surveys (Lazareff et al. 2017; GRAVITY Collaboration 2019) and implies rim temperatures of $T_{\text{rim}} \approx 2100-2200$ K for both the one-zone-plus-Gaussian and the two-zone disc models. In contrast, assuming a wall-like inner rim and a sublimation temperature of $T_{\text{rim,literature}} = 1500$ K (Dullemond & Monnier 2010) places the inner rim farther out at $R_{\text{rim,literature}} = 0.3$ au.

From this, we conclude that:

1. The circumstellar disc around HD 142527 A exhibits a complex, strongly non-point symmetric, and temporally variable geometry. Our best-fit model shows no direct connection between the separation and/or position of the azimuthal asymmetry and the stellar companion HD 142527 B. Nevertheless, the very complex state of the innermost disc region is, likely, caused by the close pass (Fig. 2) and short orbit ($P \approx 24$ yr) of the companion, which together with its large Hill radius of $R_{\text{H}} \approx 2$ au, strongly perturbs the disc ($r_{\text{out}} \lesssim 6$ au) around the primary (Sect. 5.1). This is supported by hydrodynamical simulations from Price et al. (2018).
2. We cannot fully constrain the movement of the asymmetry or explain its position given the interval between epochs ($\sim 1-1.3$ yr). This suggests that the asymmetry is intrinsically more complex (potentially involving multiple clumps or spirals), as observed in other planet-forming discs (see Setterholm et al. 2025). Further investigation would require

more sophisticated models (e.g. higher orders of modulation $\ell > 1$ for the two-zone model) or image reconstruction. However, we lack sufficient data coverage to justify these approaches.

3. The discrepancy between the spatial extent of the inner edge from the literature and our findings likely reflects one of several factors. These may include an oversimplified view of the sublimation radius (i.e. not accounting for different dust grain species, see Gail 2004), hot and dense gas (Benisty et al. 2010a), or material present farther inwards (Klarmann et al. 2017). Analysis of X-shooter spectra (Mendigutía et al. 2014; Fairlamb et al. 2015) excludes dense, hot gas as a potential source for the rim located farther inwards. We therefore conclude that the inner rim of $R_{\rm rim} \approx 0.1$ au most likely reflects a different dust composition or material farther inward.

Due to the complexity of the object, an in-depth study of the position and movement of the asymmetry likely requires more data. This could be achieved with a dedicated MATISSE imaging-style campaign using the UTs obtained during a single epoch (ideally the same night, or at least the same period) with denser sampling in (u, v) space (roughly five hour angles spaced by an hour). Additionally, observations obtained farther from the periapsis passage (e.g. around 2027, near apoapsis) could provide additional insight into the companion's effect on the disc. Finally, radial velocity measurements (e.g. with the VLT/Echelle Spectrograph for Rocky Exoplanet- and Stable Spectroscopic Observations (ESPRESSO) instrument) could constrain the orbiting speed and direction of the asymmetry.

Data availability

The code used for data analysis and plotting (incl. csv. tables), which employs the `oiplot` package (`https://zenodo.org/records/16727743`), is available at `https://zenodo.org/records/18922120`. The model-fitting code from the `ppdmod` package is available at `https://zenodo.org/records/16728341`.

Acknowledgements. We thank the anonymous referee for their constructive and detailed comments, which significantly contributed to the improvement of this work. The MATISSE consortium is composed of multiple institutes: The Côte d'Azur observatory with the J-L Lagrange laboratory, the Institut National des Sciences de l'Universe (INSU) at the Centre National de la Recherche Scientifique (CNRS), the University of Nice Sophia-Antipolis, the Max Planck Institute for Astronomy (MPIA), the Max Planck Institute for Radio Astronomy (MPIfR), the University of Kiel, the University of Leiden and the Nederlandse Onderzoekschool Voor Astronomie (NOVA), the University of Vienna, the University of Cologne, and the Konkoly observatory. GRAVITY has been developed in a collaboration by the Max-Planck-Institute for Extraterrestrial Physics, LESIA of Paris Observatory-PSL/CNRS/Sorbonne université/université Paris Cité and IPAG of Université Grenoble Alpes/CNRS, the MPIA, the university of Cologne, the Centro Multidisciplinar de Astrofisica Lisbon and Porto, and the ESO. We also acknowledge the support of M. Fousneau and the `data science group` of the MPIA for their assistance with Bayesian inference. This work was supported by CNRS/INSU, by the "Programme National de Physique Stellaire" (PNPS) of CNRS/INSU co-funded by CEA and CNES, and by Action Spécifique ASHRA of CNRS/INSU co-funded by CNES. This work has been supported by the French National Research Agency (ANR) in the framework of the "Investissements d'Avenir" program (ANR-15-IDEX-02) and in the framework of the "ANR-23-EDIR0001-01" project. J.V. is funded from the Hungarian NKFIH OTKA project no. K-132406, and K-147380. This work was also supported by the NKFIH NKKP grant ADVANCED 149943. Project no. 149943 has been implemented with the support provided by the Ministry of Culture and Innovation of Hungary from the National Research, Development and Innovation Fund, financed under the NKKP ADVANCED funding scheme. J.V. acknowledges support from the Fizeau exchange visitors programme. The research leading to these results has received funding from the European Union's Horizon 2020 research and innovation programme under Grant Agreement 101004719 (ORP). F.L. acknowledges support from the NKFIH OTKA project no. K-147380. Furthermore, this publication made use of the `National Aeronautics and Space Administration (NASA) Astrophysics Data System (ADS)`, the `Set of Identifications, Measurements and Bibliography for Astronomical Data (SIMBAD)` database, operated at Centre de Données Astronomiques de Strasbourg (CDS), and the `OiDB` of the JMMC. This work is based on observations collected at the European Southern Observatory under ESO programmes 190.C-0963(B), 190.C-0963(D), 190.C-0963(E), 190.C-0963(F) for VLTI/PIONIER; 098.D-0488(A) for VLTI/GRAVITY; and 106.21Q8.007, 108.225V.006, 108.225V.009, 108.225V.011, 111.254P.001, and 111.254P.002 for VLTI/MATISSE. In addition, we made use of data from the following surveys or libraries: the Two Micron All-Sky Survey (2MASS) (Skrutskie et al. 2006), a joint project of the university of Massachusetts and the Infrared Processing and Analysis Center (IPAC)/California Institute of Technology (Caltech), funded by NASA and the National Science Foundation (NSF); the `X-shooter spectral library` (Chen et al. 2014); the European Space Agency (ESA) mission *`Gaia`*, processed by the *Gaia* `Data Processing and Analysis Consortium (DPAC)`. Funding for the DPAC has been provided by national institutions, in particular the institutions participating in the *Gaia* multilateral agreement; and from WISE (Mainzer et al. 2011), a joint project of the University of California, Los Angeles, and the Jet Propulsion Laboratory (JPL)/Caltech, and NEOWISE (Wright et al. 2010), a project of the JPL/Caltech. WISE and NEOWISE are funded by NASA. This paper utilised the following software: the large language models (LLMs) `ChatGPT 4` (OpenAI et al. 2023), `DeepSeek-R1` (Guo et al. 2025), and `lumo 1.1` for code assistance/completion; `Aspro` of the JMMC. Furthermore, the following Python packages: `astropy` (Astropy Collaboration 2013, 2018, 2022); `astroquery` (Ginsburg et al. 2019, 2024); `corner` (Foreman-Mackey 2016; Foreman-Mackey et al. 2024); `dynesty` (Speagle 2020); `matplotlib` (Hunter 2007); `numpy` (Harris et al. 2020); `oiplot` (Scheuck 2025a); `optool` (Dominik et al. 2021); `pandas` (McKinney 2010; The pandas development Team 2025) with `openpyxl`; `ppdmod` (Scheuck 2025b); `scipy` (Virtanen et al. 2020; Gommers et al. 2025) from which the following functions were used: *j0* (wrapper of `Cephes` library), *jv* (wrapper of `AMOS` *zbesj* routine; Amos 1995), and `gaussian_kde` (Gray 1969; Bashtannyk & Hyndman 2001; Scott 2015; Silverman 2018); `SciencePlots` (Garrett et al. 2023); `tqdm` (da Costa-Luis et al. 2024). Some of the acknowledgements were compiled using the `astronomy acknowledgement generator` with some of the software citation information being aggregated using `the software citation station` (Wagg & Broekgaarden 2024; Wagg et al. 2024).

References

ALMA Partnership, Fomalont, E. B., Vlahakis, C., et al. 2015, ApJ, 808, L1
Amos, D. E. 1995, ACM Trans. Math. Softw., 21, 388
Andrae, R., Schulze-Hartung, T., & Melchior, P. 2010, arXiv e-prints [arXiv:1012.3754]
Andrews, S. M. 2020, ARA&A, 58, 483
Andrews, S. M., Huang, J., Pérez, L. M., et al. 2018, ApJ, 869, L41
Assani, K. D., Harsono, D., Ramsey, J. P., et al. 2024, A&A, 688, A26
Astropy Collaboration (Robitaille, T. P., et al.) 2013, A&A, 558, A33
Astropy Collaboration (Price-Whelan, A. M., et al.) 2018, AJ, 156, 123
Astropy Collaboration (Price-Whelan, A. M., et al.) 2022, ApJ, 935, 167
Avenhaus, H., Quanz, S. P., Schmid, H. M., et al. 2017, AJ, 154, 33
Bashtannyk, D. M., & Hyndman, R. J. 2001, Comput. Stat. Data An., 36, 279
Benisty, M., Natta, A., Isella, A., et al. 2010a, A&A, 511, A74
Benisty, M., Tatulli, E., Ménard, F., & Swain, M. R. 2010b, A&A, 511, A75
Benisty, M., Renard, S., Natta, A., et al. 2011, A&A, 531, A84
Benisty, M., Dominik, C., Follette, K., et al. 2023, ASP Conf. Ser., 534, 605
Berger, J. P., & Segransan, D. 2007, New A Rev., 51, 576
Biller, B., Lacour, S., Juhász, A., et al. 2012, ApJ, 753, L38
Birnstiel, T. 2024, ARA&A, 62, 157
Boccaletti, A., Di Folco, E., Pantin, E., et al. 2020, A&A, 637, L5
Boehler, Y., Weaver, E., Isella, A., et al. 2017, ApJ, 840, 60
Bohn, A. J., Benisty, M., Perraut, K., et al. 2022, A&A, 658, A183
Bouwman, J., Meeus, G., de Koter, A., et al. 2001, A&A, 375, 950
Buscher, D. F. 2015, Practical Optical Interferometry: Imaging at Visible and Infrared Wavelengths, Cambridge Observing Handbooks for Research Astronomers (Cambridge: Cambridge University Press)
Caratti o Garatti, A., Ray, T. P., Kavanagh, P. J., et al. 2024, A&A, 691, A134
Casassus, S., van der Plas, G. M., Perez, S., et al. 2013, Nature, 493, 191
Casassus, S., Marino, S., Pérez, S., et al. 2015, ApJ, 811, 92
Chen, Y.-P., Trager, S. C., Peletier, R. F., et al. 2014, The Messenger, 158, 30
Choi, J., Dotter, A., Conroy, C., et al. 2016, ApJ, 823, 102
Christiaens, V., Casassus, S., Absil, O., et al. 2018, A&A, 617, A37

Claudi, R., Maire, A.-L., Mesa, D., et al. 2019, A&A, 622, A96
Cohen, M., Wheaton, W. A., & Megeath, S. T. 2003, AJ, 126, 1090
Cutri, R. M., Skrutskie, M. F., van Dyk, S., et al. 2003, 2MASS All Sky Catalog of point sources
da Costa-Luis, C., Larroque, S. K., Altendorf, K., et al. 2024, `https://doi.org/10.5281/zenodo.14231923`
Dominik, C., Min, M., & Tazaki, R. 2021, Astrophysics Source Code Library [`record ascl:2104.010`]
Dorschner, J., Begemann, B., Henning, T., Jaeger, C., & Mutschke, H. 1995, A&A, 300, 503
Dullemond, C. P., & Monnier, J. D. 2010, ARA&A, 48, 205
Eggleton, P. P. 1983, ApJ, 268, 368
Fairlamb, J. R., Oudmaijer, R. D., Mendigutía, I., Ilee, J. D., & van den Ancker, M. E. 2015, MNRAS, 453, 976
Fedele, D., Carney, M., Hogerheijde, M. R., et al. 2017, A&A, 600, A72
Fitzpatrick, E. L., & Massa, D. 2009, ApJ, 699, 1209
Flock, M., Chrenko, O., Ueda, T., et al. 2025, A&A, 701, A259
Foreman-Mackey, D. 2016, JOSS, 1, 24
Foreman-Mackey, D., Price-Whelan, A., Vousden, W., et al. 2024, `https://doi.org/10.5281/zenodo.14209694`
Fukagawa, M., Tamura, M., Itoh, Y., et al. 2006, ApJ, 636, L153
Gaia Collaboration (Prusti, T., et al.) 2016, A&A, 595, A1
Gaia Collaboration (Brown, A. G. A., et al.) 2018, A&A, 616, A1
Gaia Collaboration (Brown, A. G. A., et al.) 2021, A&A, 649, A1
Gaia Collaboration (Vallenari, A., et al.) 2023, A&A, 674, A1
Gail, H.-P. 2004, A&A, 413, 571
Garrett, J., Luis, E., Peng, H.-H., et al. 2023, `https://doi.org/10.5281/zenodo.10206719`
Garufi, A., Meeus, G., Benisty, M., et al. 2017, A&A, 603, A21
Garufi, A., Benisty, M., Pinilla, P., et al. 2018, A&A, 620, A94
Ginsburg, A., Sipőcz, B. M., Brasseur, C. E., et al. 2019, AJ, 157, 98
Ginsburg, A., Sipőcz, B., Brasseur, C. E., et al. 2024, `https://doi.org/10.5281/zenodo.10799414`
Gommers, R., Virtanen, P., Haberland, M., et al. 2025, `https://doi.org/10.5281/zenodo.15716342`
GRAVITY Collaboration (Abuter, R., et al.) 2017, A&A, 602, A94
GRAVITY Collaboration (Perraut, K., et al.) 2019, A&A, 632, A53
GRAVITY Collaboration (Sanchez-Bermudez, J., et al.) 2021, A&A, 654, A97
GRAVITY Collaboration (Ganci, V., et al.) 2024, A&A, 684, A200
Gray, P. G. 1969, J. R. Stat. Soc. Series A (General), 132, 272
Guo, D., Yang, D., Zhang, H., et al. 2025, Nature, 645, 633
Guzmán-Díaz, J., Mendigutía, I., Montesinos, B., et al. 2021, A&A, 650, A182
Haffert, S. Y., Bohn, A. J., de Boer, J., et al. 2019, Nat. Astron., 3, 749
Hamilton, D. P., & Burns, J. A. 1992, Icarus, 96, 43
Harker, D. E., & Desch, S. J. 2002, ApJ, 565, L109
Harris, C. R., Millman, K. J., van der Walt, S. J., et al. 2020, Nature, 585, 357
Hauschildt, P. H., Barman, T., Baron, E., Aufdenberg, J. P., & Schweitzer, A. 2025, A&A, 698, A47
Henning, T., & Mutschke, H. 1997, A&A, 327, 743
Hunter, J. D. 2007, CSE, 9, 90
Hunziker, S., Schmid, H. M., Ma, J., et al. 2021, A&A, 648, A110
Indebetouw, R., Mathis, J. S., Babler, B. L., et al. 2005, ApJ, 619, 931
Jaeger, C., Molster, F. J., Dorschner, J., et al. 1998, A&A, 339, 904
Juhász, A., Bouwman, J., Henning, T., et al. 2010, ApJ, 721, 431
Keppler, M., Benisty, M., Müller, A., et al. 2018, A&A, 617, A44
Klarmann, L., Benisty, M., Min, M., et al. 2017, A&A, 599, A80
Kluska, J., Van Winckel, H., Coppée, Q., et al. 2022, A&A, 658, A36
Lacour, S., Biller, B., Cheetham, A., et al. 2016, A&A, 590, A90
Lazareff, B., Berger, J.-P., Kluska, J., et al. 2017, A&A, 599, A85
Lopez, B., Lagarde, S., Petrov, R. G., et al. 2022, A&A, 659, A192
Mainzer, A., Bauer, J., Grav, T., et al. 2011, ApJ, 731, 53
Marino, S., Perez, S., & Casassus, S. 2015, ApJ, 798, L44
Matter, A., Labadie, L., Kreplin, A., et al. 2014, A&A, 561, A26
McKinney, W. 2010, SciPy 2010
Mendigutía, I., Fairlamb, J., Montesinos, B., et al. 2014, ApJ, 790, 21
Menu, J., van Boekel, R., Henning, T., et al. 2015, A&A, 581, A107
Millour, F., Berio, P., Heininger, M., et al. 2016, SPIE Conf. Ser., 9907, 990723
Min, M., Hovenier, J. W., & de Koter, A. 2005, A&A, 432, 909
Min, M., Waters, L. B. F. M., de Koter, A., et al. 2007, A&A, 462, 667
Müller, A., Keppler, M., Henning, T., et al. 2018, A&A, 617, L2
Nowak, M., Rowther, S., Lacour, S., et al. 2024, A&A, 683, A6
OpenAI, Achiam, J., Adler, S., et al. 2023, arXiv e-prints [arXiv:`2303.08774`]
Paunzen, E. 2022, A&A, 661, A89
Petrov, R. G., Allouche, F., Matter, A., et al. 2020, SPIE Conf. Ser., 11446, 114460L
Pinte, C., van der Plas, G., Ménard, F., et al. 2019, Nat. Astron., 3, 1109
Pohl, A., Benisty, M., Pinilla, P., et al. 2017, ApJ, 850, 52
Price, D. J., Cuello, N., Pinte, C., et al. 2018, MNRAS, 477, 1270
Riello, M., De Angeli, F., Evans, D. W., et al. 2021, A&A, 649, A3
Rubinstein, A. E., Macías, E., Espaillat, C. C., et al. 2018, ApJ, 860, 7
Rufener, F., & Nicolet, B. 1988, A&A, 206, 357
Scheuck, M. B. 2025a, `https://doi.org/10.5281/zenodo.16727743`
Scheuck, M. B. 2025b, `https://doi.org/10.5281/zenodo.16728341`
Scott, D. W. 2015, Multivariate Density Estimation: Theory, Practice, and Visualization, 1st edn., Wiley Series in Probability and Statistics (Hoboken: Wiley)
Setterholm, B. R., Monnier, J. D., Baron, F., et al. 2025, AJ, 169, 318
Silverman, B. 2018, Density Estimation for Statistics and Data Analysis, 1st edn. (UK: Routledge)
Skilling, J. 2004, AIP Conf. Ser., 735, 395
Skrutskie, M. F., Cutri, R. M., Stiening, R., et al. 2006, AJ, 131, 1163
Sogawa, H., Koike, C., Chihara, H., et al. 2006, A&A, 451, 357
Speagle, J. S. 2020, MNRAS, 493, 3132
Teague, R., Bae, J., Bergin, E. A., Birnstiel, T., & Foreman-Mackey, D. 2018, ApJ, 860, L12
The pandas development Team. 2025, `https://doi.org/10.5281/zenodo.15597513`
van Boekel, R., Min, M., Leinert, C., et al. 2004, Nature, 432, 479
van Boekel, R., Min, M., Waters, L. B. F. M., et al. 2005, A&A, 437, 189
Varga, J., Ábrahám, P., Chen, L., et al. 2018, A&A, 617, A83
Varga, J., Hogerheijde, M., van Boekel, R., et al. 2021, A&A, 647, A56
Varga, J., Waters, L. B. F. M., Hogerheijde, M., et al. 2024, A&A, 681, A47
Vioque, M., Oudmaijer, R. D., Baines, D., Mendigutía, I., & Pérez-Martínez, R. 2018, A&A, 620, A128
Virtanen, P., Gommers, R., Oliphant, T. E., et al. 2020, Nat. Me., 17, 261
Wagg, T., & Broekgaarden, F. S. 2024, arXiv e-prints [arXiv:`2406.04405`]
Wagg, T., Broekgaarden, F., & Gültekin, K. 2024, Zenodo, `https://doi.org/10.5281/zenodo.13225824`
Woillez, J., Petrov, R., Abuter, R., et al. 2024, A&A, 688, A190
Wright, E. L., Eisenhardt, P. R. M., Mainzer, A. K., et al. 2010, AJ, 140, 1868
Zubko, V. G., Mennella, V., Colangeli, L., & Bussoletti, E. 1996, MNRAS, 282, 1321

Appendix A: Observations

Table A.1: The HD 142527 observations used in this study.

HD 142527						Calibrator				
Date and Time (UTC)	Instrument	Seeing ($''$)	τ_0 (ms)	Array: Stations	Band	ΔTime (h:mm)	Name	LDD (mas)	Seeing ($''$)	τ_0 (ms)
2013-02-20T08:14[†]	PIONIER	0.8	3.1	M: D0-G1-H0-I1	H	∼±20	HD142135	0.42	0.7	4.0
2013-06-04T04:53[†#]	PIONIER	1.2	3.7	L: K0-A1-G1-J3	H	–	–	–	–	–
2013-06-06T02:16[†#]	PIONIER	1.1	3.8	L: K0-A1-G1-J3	H	–	–	–	–	–
2013-06-07T01:39[†#]	PIONIER	0.8	7.4	L: K0-A1-G1-J3	H	–	–	–	–	–
2013-06-10T01:08[†#]	PIONIER	0.9	5.3	L: K0-A1-G1-J3	H	–	–	–	–	–
2013-06-15T02:57[†]	PIONIER	1.4	2.2	M: D0-G1-H0-I1	H	∼±20	HD 142386	0.24	1.3	1.3
2013-07-03T01:16[†#]	PIONIER	1.4	2.7	S: D0-A1-C1-B2	H	–	–	–	–	–
2017-03-19T08:51[††]	GRAVITY	0.7	8.0	L: A0-G1-J2-K0	K	+1:18	HD 143118	0.37	0.8	4.9
2019-03-23T09:06[‡]	MATISSE	0.5	10.8	S: A0-B2-D0-C1	L	+0:13	* eps Sco	5.8	0.4	11.3
2019-05-06T04:00[‡]	MATISSE	0.5	5.8	L: K0-G1-D0-J3	L	−0:13	HD 138742	1.2	0.7	5.6
2019-06-30T04:49	MATISSE	0.9	1.8	S: A0-B2-D0-C1	L	+0:30	* eps Sco	5.8	1.5	1.7
2021-03-08T07:52[‡]	MATISSE	1.1	3.8	L: A0-G1-J2-J3	L	−0:27	HD139127	3.2	1.8	3.0
2021-03-11T06:47[‡]	MATISSE	0.7	8.4	M: K0-G2-D0-J3	L	−0:26	HD139127	3.2	0.8	6.4
2021-03-16T06:50[‡]	MATISSE	1.0	2.5	S: A0-B2-D0-C1	L	+0:26	* H Sco	4.7	1.4	1.7
2021-03-27T05:29	MATISSE	1.0	5.7	U: U1-U2-U3-U4	LN	−0:31	HD134505	2.5	1.0	7.3
2022-03-14T06:48	MATISSE	0.9	4.1	S: A0-B2-D0-C1	L	+0:26	* H Sco	4.7	0.8	4.1
2022-03-23T08:20	MATISSE	0.6	4.1	U: U1-U2-U3-U4	LN	−0:31	HD138816	2.1	0.7	3.8
2022-05-11T06:22	MATISSE	1.2	2.9	L: A0-G1-J2-J3	L	+0:29	HD149401	2.5	1.0	3.3
2023-05-14T04:25	MATISSE	0.8	4.4	S: A0-B2-D0-C1	L	−0:41	* ups Lib	4.6	1.4	2.8
2023-06-12T04:10[‡]	MATISSE	0.7	2.5	S: A0-B2-D0-C1	L	−0:27	* ups Lib	4.6	0.8	3.4
2023-07-01T00:57	MATISSE	1.0	4.8	U: U1-U2-U3-U4	LN	−0:24	HD134505	2.5	1.2	4.5
2023-07-09T03:53	MATISSE	0.6	2.8	S: A0-B2-D0-C1	L	−0:27	* ups Lib	4.6	0.6	3.3
2023-07-12T00:36	MATISSE	1.6	0.8	S: A0-B2-D0-C1	L	−0:34	* ups Lib	4.6	1.8	1.3
2023-08-12T01:32	MATISSE	0.9	3.2	S: A0-B2-D0-C1	L	−0:28	* ups Lib	4.6	1.3	3.1

Notes. *Columns*: Instrument, date and time, atmospheric conditions (seeing and coherence time τ_0), array configurations and corresponding stations, spectral band, and information on the calibrator. Observations highlighted in red were not used. Letters in the 'Array: Stations' column are abbreviations of the various configurations (i.e. 'S' – small, 'M' – medium, 'L' – large, and 'U' – UTs). For HD 142527, seeing and coherence time τ_0 are the mean value during observations, while for the calibrator they are the value obtained at the beginning of observations.
(†)Archival data obtained from OiDB (Lazareff et al. 2017). (††)Reduced and calibrated data obtained from GRAVITY Collaboration (2019). (#)No calibrator information logged for this observation. (‡)Although good atmospheric conditions, artifacts or a low S/N is present.

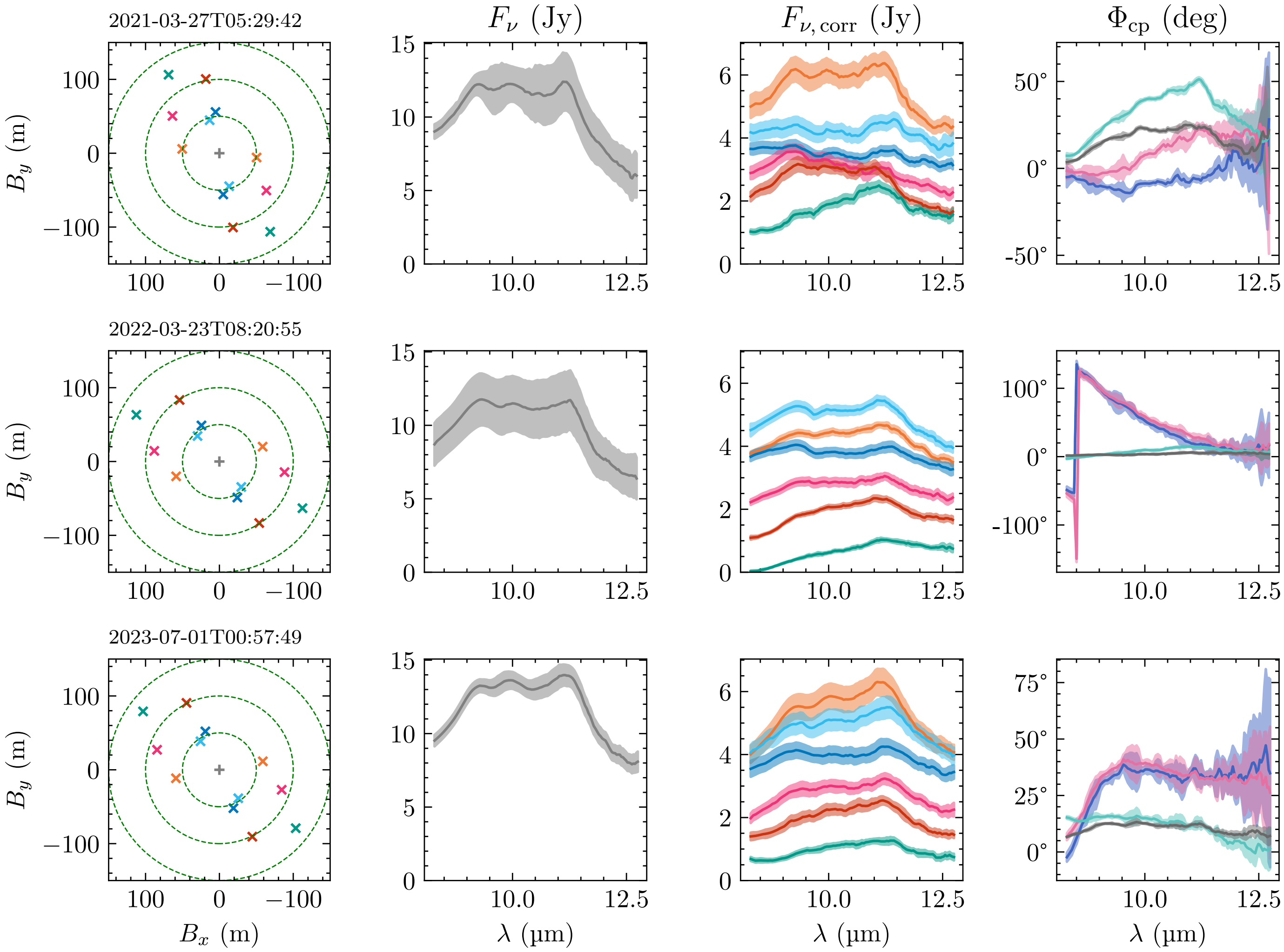

Fig. A.1: MATISSE *N*-band observations of HD 142527 (Table A.1). *Left to right*: Baseline distribution (B_x, B_y), single dish spectra F_ν, correlated fluxes $F_{\nu,\mathrm{corr}}$, and closure phases $\Phi_{\nu,\mathrm{cp}}$.

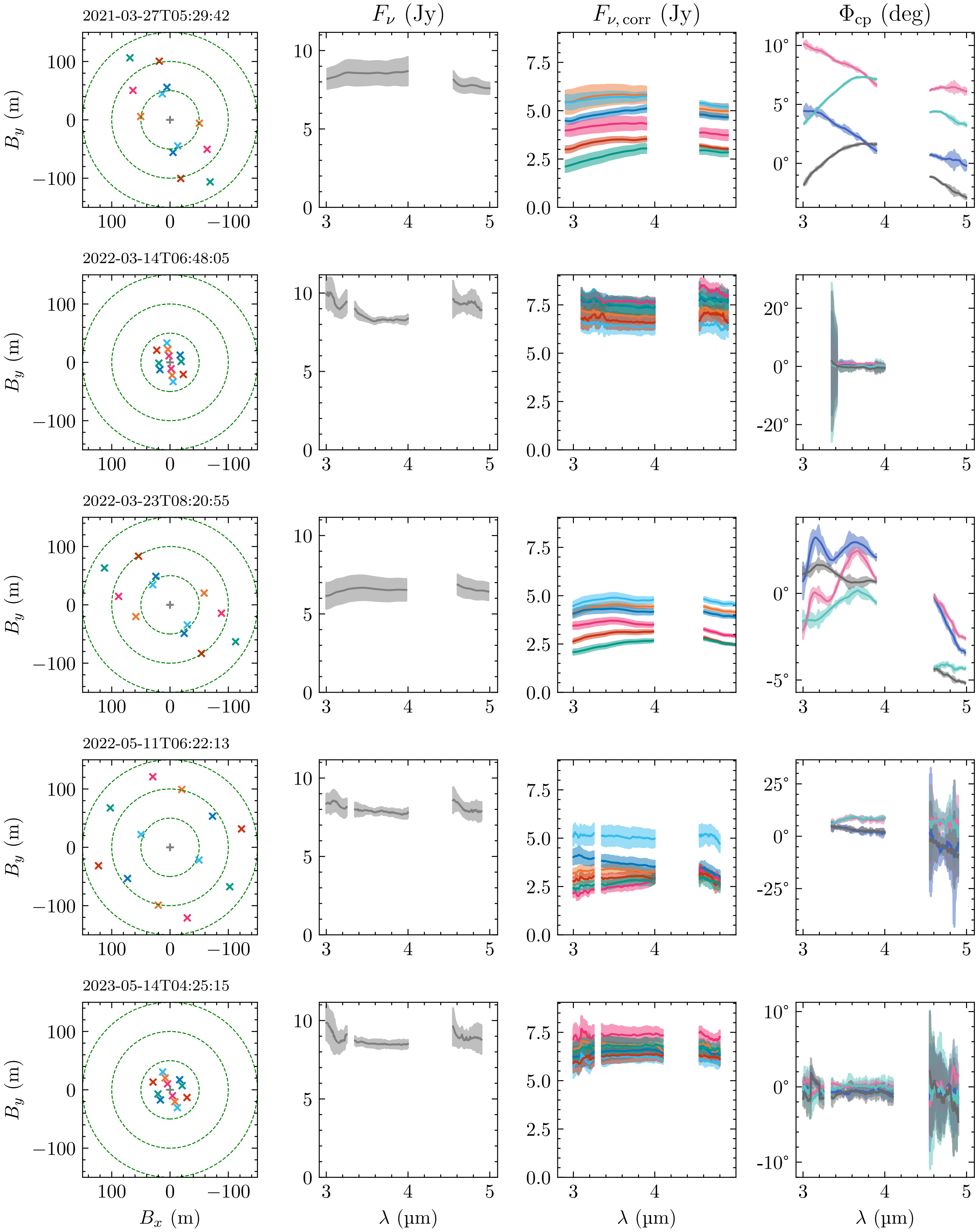

Fig. A.2: Individual *L*/*M*-band, MATISSE observations of HD 142527 (Table A.1). Layout is identical as for Fig. A.1. Single-dish spectra originate from chopped mode, with the other observables from non-chopped mode. Emission peaks not relevant to this study, poor-quality data, and ranges outside the band windows were flagged and are not shown.

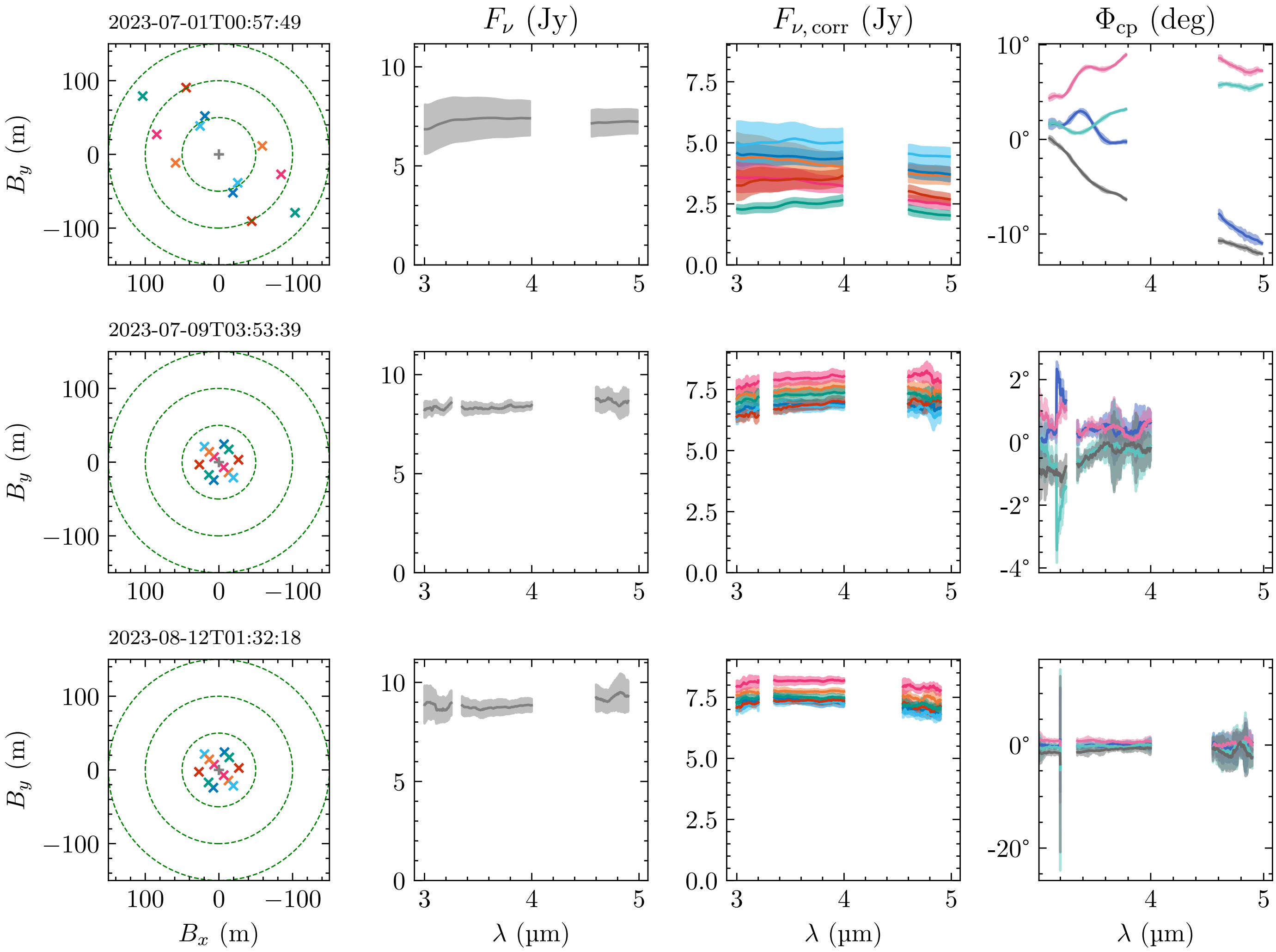

Fig. A.3: Continuation of Fig. A.2

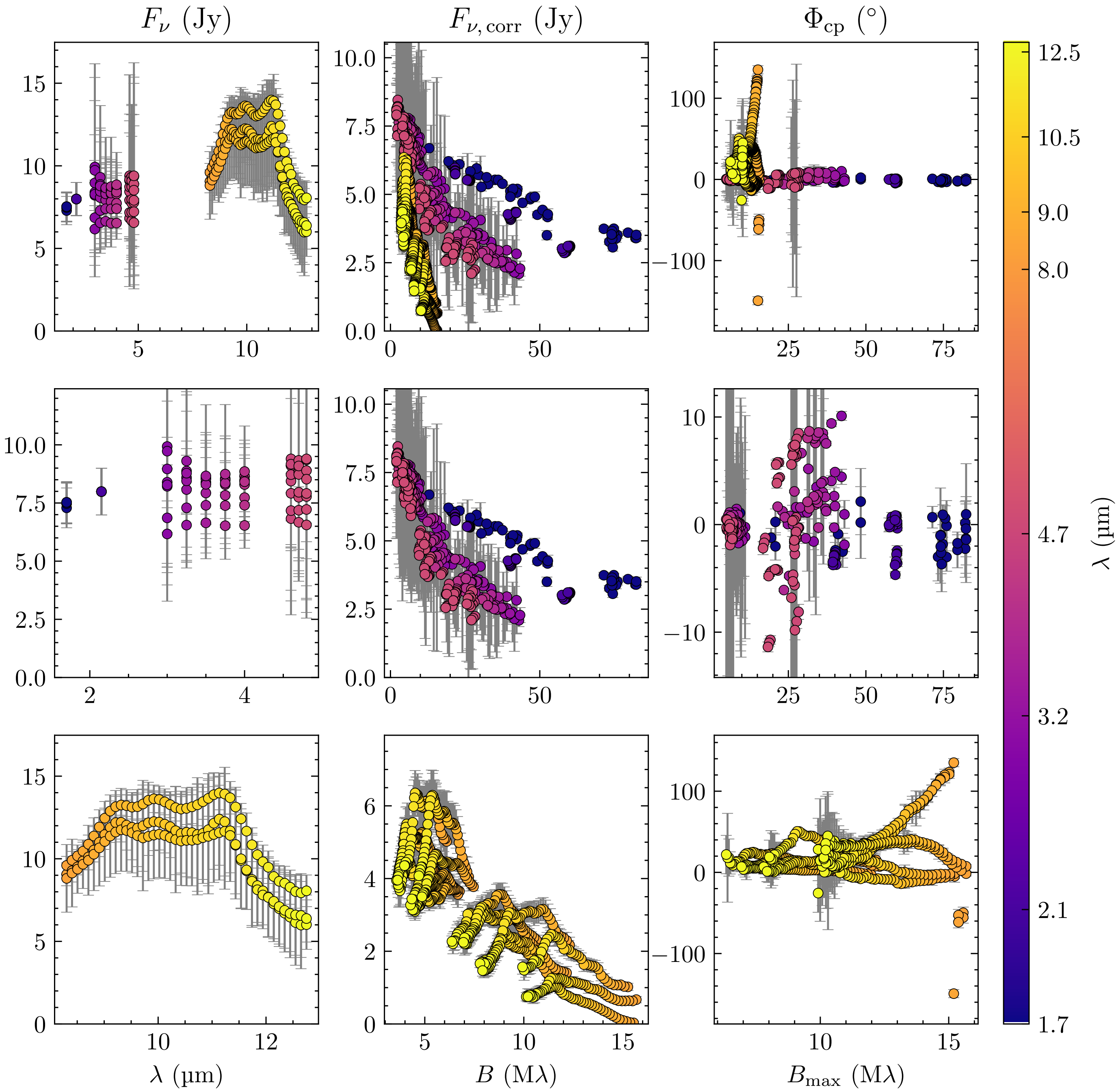

Fig. A.4: Overview of binned data used for model-fitting. *Left to right*: Single dish spectra F_ν, correlated fluxes $F_{\nu,\mathrm{corr}}$, and closure phases $\Phi_{\nu,\mathrm{cp}}$. *Top to bottom*: Data from *H*-*N* bands, a zoom-in to the *H*-*M* bands, and a zoom-in to the *N* band.

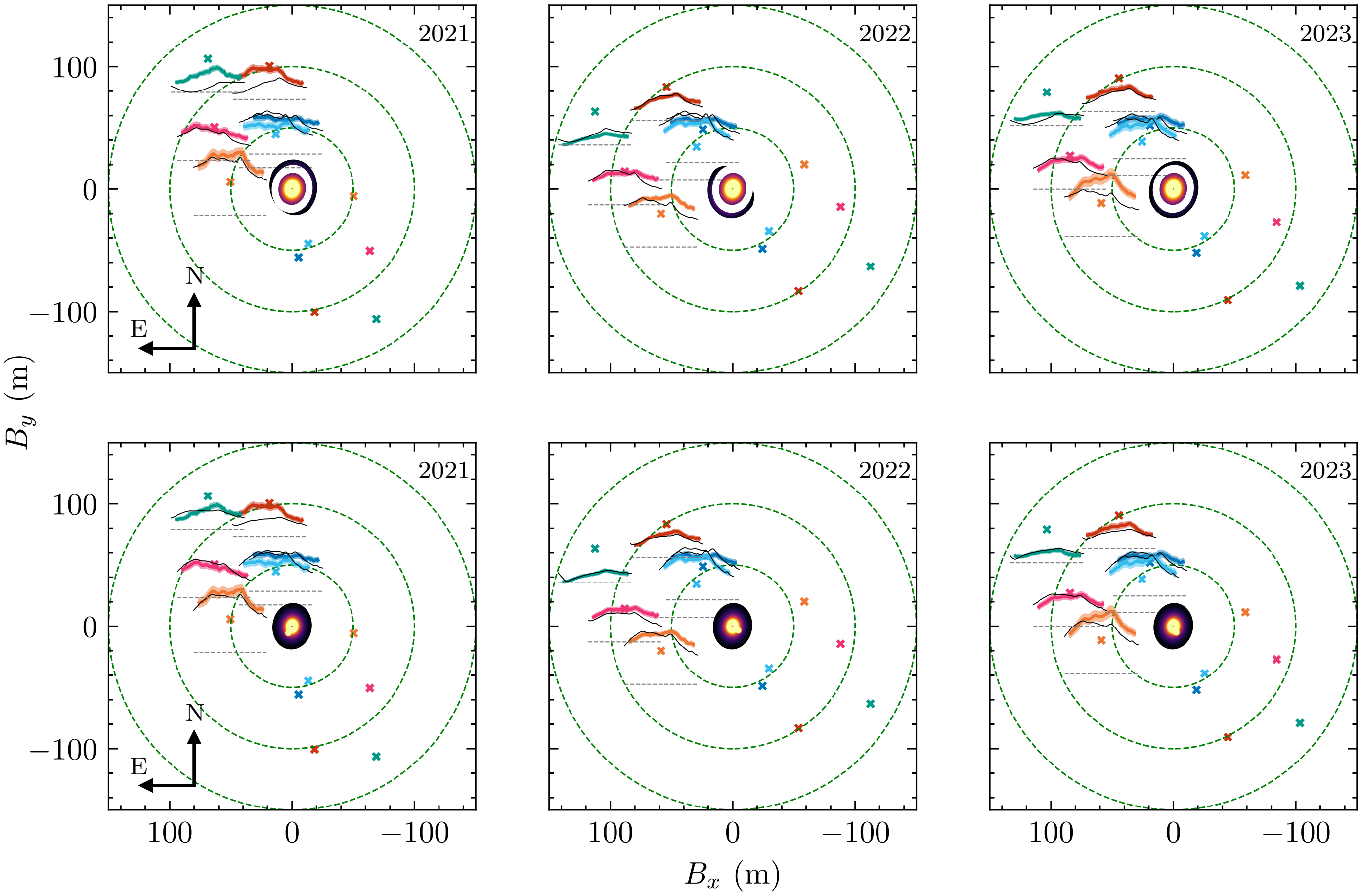

Fig. A.5: Baseline distribution (B_x, B_y) of all N-band epochs. Each plot shows correlated fluxes $F_{\nu,\mathrm{corr}}$ (coloured lines) in its top-left corner overlaid with the model (black lines) at baseline positions (coloured crosses) and equidistant baseline contours (green-dashed circles; 50 m step-width). Additionally, zero lines of the y-axis (grey-dashed lines) correspond to the correlated flux curves. *Left to right*: Three N-band epochs (2021, 2022, and 2023). *Top*: Two-zone disc model. *Bottom*: One-zone disc model with a Gaussian.

Appendix B: Model fitting

We chose Bayesian inference, more specifically nested sampling, to fit our model to the data. Nested sampling efficiently explores the probability distribution of the parameter space (even if not well-defined; typically problematic with Markov Chain Monte Carlo (MCMC) methods). It estimates the evidence

$$\mathcal{Z} \equiv P(\boldsymbol{D}|M) = \int_0^\infty X(x)\,\mathrm{d}x = \int \mathcal{L}(X)\,\mathrm{d}X, \tag{B.1}$$

by treating the integral of the posterior over all parameters as an integral over the prior volume

$$X(x) = \int_{\boldsymbol{\Theta}:\mathcal{L}(\boldsymbol{\Theta})>x} \pi(\boldsymbol{\Theta})\,\mathrm{d}\boldsymbol{\Theta} \tag{B.2}$$

instead. Then, the iso-likelihood contour $\mathcal{L}_i = \mathcal{L}(X_i)$ associated with samples is evaluated from the prior volume and the evidence computed over 'nested' shells. At each iteration i, the remaining evidence in the prior volume is roughly bounded by $\Delta\mathcal{Z}_i \approx \mathcal{L}_{\max} X_i$. The difference between remaining and current evidence $\mathcal{Z}_i$,

$$\Delta \ln \mathcal{Z}_i \equiv \ln\left(\mathcal{Z}_i + \Delta\mathcal{Z}_i\right) - \ln \mathcal{Z}_i, \tag{B.3}$$

serves as the stopping criterion (Skilling 2004; Speagle 2020).

We use the least-squares minimisation for the likelihood

$$\mathcal{L}(\boldsymbol{\Theta}) \equiv P(\boldsymbol{D}|\boldsymbol{\Theta}, M) \equiv \chi^2(\boldsymbol{\Theta}) = \sum_{n=1}^{N} \left(\frac{y_n - M(\boldsymbol{\Theta})}{\sigma_n}\right)^2, \tag{B.4}$$

enabling the fitting of a model to data of N points y_n measured with (uncorrelated) errors σ_n. Estimating the fit-goodness and for model comparison, we also use the reduced form:

$$\chi^2_{\mathrm{r}}(\boldsymbol{\Theta}) = \frac{\mathcal{L}(\boldsymbol{\Theta})}{N - N_{\boldsymbol{\Theta}}}, \tag{B.5}$$

which takes the degrees of freedom (DOF) $N - N_{\boldsymbol{\Theta}}$ into account (Andrae et al. 2010). The number of model parameters $N_{\boldsymbol{\Theta}}$ may vary between epochs (i.e. time-variable parameters) and/or for each observable.

The likelihood $\mathcal{L}$ consists of contributions from the total spectra, the correlated fluxes, and the closure phases, which are computed separately and subsequently summed up:

$$\mathcal{L}_{\mathrm{tot}} = w_{F_\nu}\mathcal{L}_{F_\nu} + w_{F_{\nu,\mathrm{corr}}}\mathcal{L}_{F_{\nu,\mathrm{corr}}} + w_{\Phi_{\nu,\mathrm{cp}}}\mathcal{L}_{\Phi_{\nu,\mathrm{cp}}}. \tag{B.6}$$

However, the total reduced least squares $\chi^2_{\mathrm{r,tot}}$ is generally not a simple addition as DOF for the whole model need to be taken into account.

We only use the weights w, to achieve an equal contribution of the observables in respect to their amount of data points. Interferometric instruments at the VLTI have, per observation and frequency element ν, the following distribution of data points for each observable

$$\begin{aligned} n_{\nu,F_\nu} &= N \vee 1, \\ n_{\nu,F_{\nu,\mathrm{corr}}} &= \frac{N(N-1)}{2}, \quad \text{with} \quad \binom{N}{2}, \\ n_{\nu,\Phi_{\nu,\mathrm{cp}}} &= \frac{N(N-1)(N-2)}{6}, \quad \text{with} \quad \binom{N}{3}. \end{aligned} \tag{B.7}$$

Here, n_{ν,F_ν} is the number of single-dish spectra (often averaged; i.e. $n_{\nu,F_\nu} = 1$), $n_{\nu,F_{\nu,\mathrm{corr}}}$ the number of correlated fluxes, and $n_{\nu,\Phi_{\nu,\mathrm{cp}}}$ the number of closure phases, with N being the number of telescopes.

Appendix C: Model parameters

Table C.1: Model parameters.

Parameter	Unit	Description
Dust opacity model		
Free		
s		Scaling factor
T_{c}	(K)	Charac. temperature
$\kappa_{\nu,\mathrm{abs},k}$ [a]	$(\mathrm{cm^2\,g^{-1}})$	Absorption opacity
w_k		Opacity weight
Stellar spectrum model		
Free		
θ	(mas)	Apparent diameter
A_{V}	(mag)	V-band extinction
Fixed		
$T_\star$	(K)	Temperature
A_λ	(mag)	Extinction
g	$(\mathrm{m\,s^{-2}})$	Surface gravity
Asymmetric disc		
Free		
$R_{\mathrm{in},n}$ [b]	(au)	Inner radius
$R_{\mathrm{out},n}$	(au)	Outer radius
$w_{\mathrm{cont},n}$		Continuum weight
$\Sigma_{0,n}$	$(\mathrm{g\,cm^{-2}})$	Σ_n at R_0
p_n		Σ_n exponent
T_0	(K)	T at R_0
q		T exponent
$A_{n,m}$ [c]		Modulation amp.
$\phi_{n,m}$	(°)	Modulation angle
Fixed		
i_{in}	(°)	Inclination angle
θ_{in}	(°)	Position angle
R_0	(au)	Reference radius
$\kappa_{\nu,\mathrm{abs,sil}}$	$(\mathrm{cm^2\,g^{-1}})$	Silicate opacity
$\kappa_{\nu,\mathrm{abs,cont}}$	$(\mathrm{cm^2\,g^{-1}})$	Continuum opacity
Gaussian		
Free		
f		Scaling factor
ρ	(au)	Radial position
Φ	(°)	Position angle
Σ	$(\mathrm{g\,cm^{-2}})$	Surface density
Fixed		
a	(au)	FWHM

Notes. (a)Dust stoichiometries denoted by k. (b)Disc zones denoted by n. (c)Modulation orders denoted by m.

Appendix D: Stellar spectrum and parameters

To estimate the contribution of the stellar photosphere to our observed signals, we perform model atmosphere fitting to optical photometry of HD 142527. We use the effective temperature $T_\star = 6500\,\mathrm{K}$ derived by Fairlamb et al. (2015), from X-shooter spectroscopy, and use their spectroscopically derived surface gravity of $\log g = 3.93$ as an initial value. We calculate synthetic photometry from a reddened `PHOENIX` model spectrum by Hauschildt et al. (2025), with the corresponding parameters adopting solar composition. Then, we tune the apparent stellar diameter θ and the V-band extinction A_V, calculating synthetic photometry until reaching the best photometry fit through χ^2 minimisation, while keeping $T_\star$ and $\log g$ fixed. Adopting the GAIA distance, we then obtain an estimate of the stellar radius and luminosity. We compare these values to pre-main-sequence (PMS), evolutionary tracks by Choi et al. (2016) to obtain an estimate of the stellar mass and age. From the stellar radius and mass estimate, we retrieve an updated estimate of the surface gravity, and iteratively repeat the procedure using a `PHOENIX` model spectrum with the new $\log g$ value. Ultimately, we achieve a best-fit, reddened model atmosphere spectrum, and a set of stellar parameters that are mutually consistent. The procedure is described in detail below.

D.1. Method details

We adopt optical photometry in the Geneva system from Paunzen (2022) and from GAIA data release 3 (*Gaia* DR3) (Gaia Collaboration 2016, 2023). We also consider infrared photometry from the 2MASS point-source (Skrutskie et al. 2006; Cutri et al. 2003) and ALLWISE (Wright et al. 2010; Mainzer et al. 2011) catalogues. However, these are ignored in the fit to the photosphere as they contain infrared excess emission from the circumstellar material. We adopt the spectro-photometric response curves R_λ for the Geneva system from Rufener & Nicolet (1988), for *Gaia* DR3 from Riello et al. (2021), for 2MASS from Cohen et al. (2003), and for ALLWISE from Wright et al. (2010). The photometric zero-point (i.e. $\phi_{\lambda,0}$ for the respective bands) computation is done as follows. For the Geneva system, we use the `alpha_lyr_mod_002.fits` model spectrum from the CALSPEC database[9] and the α Lyr magnitudes from Table 11 of Rufener & Nicolet (1988); for *Gaia* DR3 we adopt the `alpha_lyr_mod_002.fits` from the CALSPEC database, scaled to $3.622\,86 \cdot 10^{-11}\,\mathrm{W\,m^{-2}\,nm^{-1}}$ at 550 nm, following Riello et al. (2021); for 2MASS we use a spectrum constant wF_λ at $3.129 \cdot 10^{-13}$, $1.133 \cdot 10^{-13}$, and $4.283 \cdot 10^{-14}\,\mathrm{W\,m^{-2}\,\mu m^{-1}}$ for the J, H, K bands, respectively, following Cohen et al. (2003); and for the ALLWISE catalog we use an α Lyr model by Martin Cohen, (Wright, private communication). All photometric facilities have detectors that are based on the photoelectric effect:

$$m_i = -2.5 \log_{10} \left(\frac{\int_0^\infty \phi_\lambda R_\lambda \,\mathrm{d}\lambda}{\int_0^\infty \phi_{\lambda,0} R_\lambda \,\mathrm{d}\lambda} \right), \tag{D.1}$$

where m_i is the observed magnitude in photometric band i, ϕ_λ is the target spectrum expresses as photon flux (e.g. $[\gamma] = [\mathrm{s^{-1}\,cm^{-2}\,\mu m^{-1}}]$), and $\phi_{\lambda,0}$ is the corresponding spectrum that defines the photometric zero point of the respective band.

The model photosphere spectrum ϕ_λ is calculated as follows:

$$\phi_\lambda = \Omega I_{\lambda,0}(T_\star, \log g) \cdot 10^{-0.4 A_\lambda}, \tag{D.2}$$

where $I_{\lambda,0}$ is the disc-integrated average surface brightness of the `PHOENIX` stellar model atmosphere without foreground extinction, $\Omega = \pi\theta^2/4$ is the solid angle subtended by the star as viewed from Earth, and A_λ is the wavelength-dependent extinction curve adopted from Indebetouw et al. (2005) and Fitzpatrick & Massa (2009), scaled so that its value at 0.55 µm matches the fit parameter A_V.

Note that in our photometric data, we measure the combined signal of the primary Herbig Ae star and the low-mass M-type companion, ignoring the contribution of the latter in our analysis. Given the much lower luminosity and photospheric temperature of the companion compared to the primary, its emission should affect the optical fluxes at no more than ≈ 1 %.

D.2. Fit results

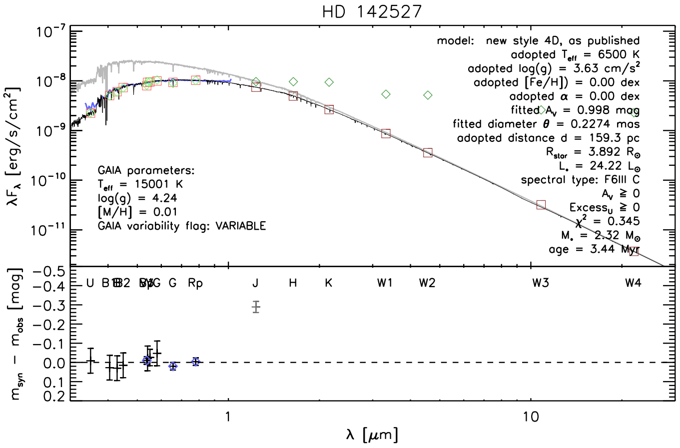

Fig. D.1: SED fit. *Top*: Best-fit stellar atmosphere model (black) overlaid with the zero-extinction model (grey), fitted to the observed photometry (green diamond) and the low-resolution GAIA XP spectrum (blue). The observed photometry is contrasted by the synthetic photometry (red squares). *Bottom*: Residuals of observed and synthetic magnitudes.

Figure D.1 shows the model atmosphere fit, with excess emission at near- and mid-IR wavelengths, as seen from divergence in observed and synthetic photometry. No scaling has been applied to the low-resolution GAIA XP spectrum, and the excellent match in flux levels illustrates both the validity of our method and the excellent absolute calibration of the GAIA spectra.

We find an adequate fit to the spectrum when using the spectroscopically derived temperature $T_\star = 6500\,\mathrm{K}$ from Fairlamb et al. (2015) with the V-band extinction $A_\mathrm{V,fit} \approx 1.0\,\mathrm{mag}$ significantly different from $A_\mathrm{V} \approx 0\,\mathrm{mag}$ of this earlier work. Consequently, we derive a substantially larger stellar radius $R_\star \approx 3.9\,\mathrm{R_\odot}$, compared to $R_\star \approx 2.2\,\mathrm{R_\odot}$ found by Fairlamb et al. (2015), and we find a correspondingly higher luminosity $L_\star \approx 24\,\mathrm{L_\odot}$. We compare this to PMS evolutionary tracks yielding a mass estimate of $M_\star \approx 2.3\,\mathrm{M_\odot}$ and an age of ≈ 3.4 Myr (i.e. an object substantially more massive and younger than $\approx 1.6\,\mathrm{M_\odot}$ and ≈ 8.1 Myr, as found by Fairlamb et al. 2015). A model with $T_\star = 6500\,\mathrm{K}$ and $A_\mathrm{V} \approx 0\,\mathrm{mag}$, as derived by Fairlamb et al. (2015), yields too blue a spectrum to be consistent with the observed optical photometry (grey curve; Fig. D.1).

---

[9] Available at `https://www.stsci.edu/hst/instrumentation/reference-data-for-calibration-and-tools/astronomical-catalogs/calspec`.

Nowak et al. (2024) find a combined mass of ≈ 2.3 $M_\odot$ for the HD 142527 A and B system from an astrometrically measured orbit fit. Mass estimates for the companion range from ≈ 0.13 – 0.34 $M_\odot$ (Lacour et al. 2016; Christiaens et al. 2018). Our combined mass estimate is somewhat higher than the one derived from the astrometric orbit.

Appendix E: Dust opacity model

Table E.1: Best-fit parameters to the averaged, N-band single-dish spectrum.

Parameter	Unit	Value
$\log(s/\mathrm{sr})$		$17.18^{+0.07}_{-0.24}$
w_{PAH}		$1.28^{+1.31}_{-1.20}$
T_{c}	(K)	$420.98^{+23.36}_{-57.21}$
w_{cont}	(%)	$69.38^{+16.85}_{-3.65}$
$w_{\mathrm{large,\,enst}}$	(%)	$2.54^{+53.41}_{-0.81}$
$w_{\mathrm{small,\,enst}}$	(%)	$5.91^{+16.87}_{-5.56}$
$w_{\mathrm{large,\,forst}}$	(%)	$2.10^{+19.92}_{-1.97}$
$w_{\mathrm{small,\,forst}}$	(%)	$5.64^{+5.87}_{-5.50}$
$w_{\mathrm{large,\,oliv}}$	(%)	$6.52^{+7.64}_{-6.52}$
$w_{\mathrm{small,\,pyrox}}$	(%)	$1.37^{+8.13}_{-1.37}$
$w_{\mathrm{large,\,sil}}$	(%)	$7.73^{+3.44}_{-7.73}$
$w_{\mathrm{small,\,sil}}$	(%)	$1.70^{+1.42}_{-1.70}$
χ^2_{r}		0.03

Notes. Over-fitting ($\chi^2_{\mathrm{r}} < 1$) is caused by the single, averaged dataset with many DOF. The weights for the silicate stoichiometries (i.e. excluding w_{cont} and w_{PAH}) are normed.

We analyse the composition of the prominent N-band silicate emission feature of HD 142527 by fitting a model to the N-band single-dish spectrum. The single-dish N-band spectroscopic data are comprised of the average of the spectra from the three MATISSE UT epochs. With the methodology and dust species of van Boekel et al. (2005), we describe the observed spectrum as a blackbody source function $B_\nu(T)$ at characteristic temperature T_{c} multiplied by a weighted sum of the absorption opacities and a polycyclic aromatic hydrocarbon (PAH) flux contribution:

$$\begin{aligned} F_{\nu,\mathrm{model}} &= (F_{\nu,\mathrm{sil}} + F_{\nu,\mathrm{cont}}) + w_{\mathrm{PAH}} F_{\mathrm{PAH}} \\ &= s B_\nu(T_{\mathrm{c}}) \sum_{\mathrm{k}} w_k \kappa_{\nu,\mathrm{abs},k} + w_{\mathrm{PAH}} F_{\nu,\mathrm{PAH}} \end{aligned} \tag{E.1}$$

Here, free parameters are the dust-stoichiometry weights w, the PAH weight w_{PAH}, T_{c}, and the scale factor s. The PAH flux F_{PAH} is an empirical PAH spectral template adopted from van Boekel et al. (2005). Each dust stoichiometry one weight per grain size (i.e. 0.1 and 2 µm). The absorption opacities $\kappa_{\nu,\mathrm{abs},k}$ are computed with `optool`[10], using the distribution of hollow spheres (DHS) (Min et al. 2005) method. Absorption opacities of the Gaussian random field (GRF) method (Min et al. 2007) were provided by M. Min. Fig. E.1 and Table E.2 show individual dust stoichiometries and structures.

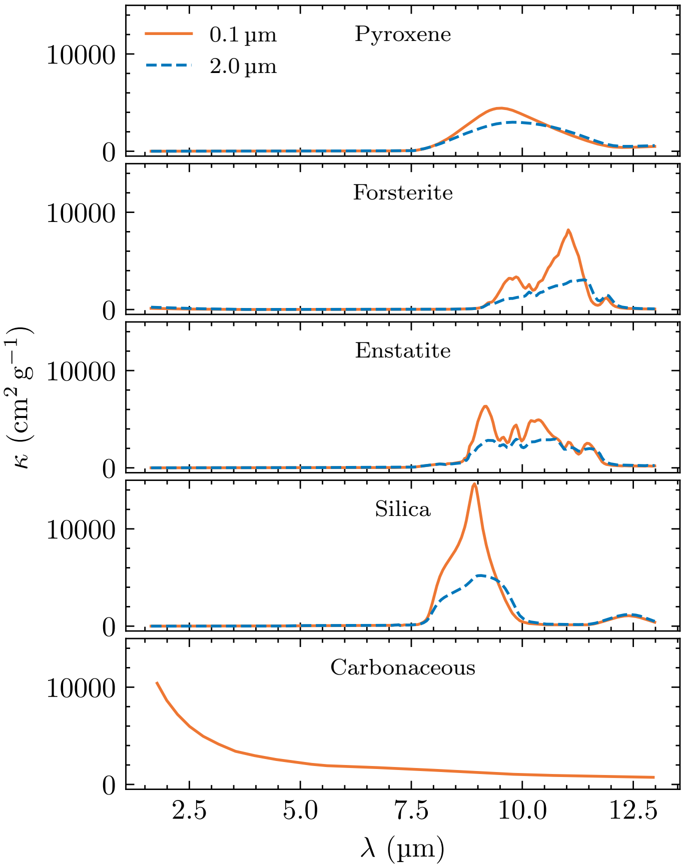

Fig. E.1: Mass absorption coefficients of dust stoichiometries. Table E.2 shows types (amorphous or crystalline) and chemical formulas. Coefficients are used in modelling the opacity contributions of HD 142527 (Sect. 4.1).

We chose amorphous carbonaceous grains for the continuum component, as they have no emission features in our wavelength range. Other species (e.g. iron) may present a valid alternative.

Decoupling the opacities (Eq. 4) enables a unique silicate-to-carbonaceous ratio for the disc component (Sect. 4.2.2). This fit method yields a reasonable, albeit imperfect, approximation of the N-band silicate opacity (see Fig. 1). We replace the silicate feature of the best-fit model with that from the observed data, using

$$\kappa_{\nu,\mathrm{abs,sil}} = \frac{F_\nu}{s B_\nu(T_{\mathrm{c}})} - \kappa_{\nu,\mathrm{abs,cont}}, \tag{E.2}$$

as we do not focus on quantitative dust spectroscopy.

---

[10] Available at https://github.com/cdominik/optool

Table E.2: Dust stoichiometries used in this work.

Stoichiometric (Grain) Type	Lattice Structure	Chemical Formula	Method	Grain Sizes	Reference
Pyroxene	Amorphous	$Mg_xFe_{1-x}SiO_3$	GRF	0.1, 2.0	(1)
Forsterite	Crystalline	Mg_2SiO_4	GRF	0.1, 2.0	(2)
Enstatite	Crystalline	$MgSiO_3$	GRF	0.1, 2.0	(3)
Silica	Crystalline	SiO_2	GRF	0.1, 2.0	(4)
Carbonaceous	Amorphous	C	DHS	0.1	(5)

References. (1) Dorschner et al. (1995); (2) Sogawa et al. (2006); (3) Jaeger et al. (1998); (4) Henning & Mutschke (1997); (5) Zubko et al. (1996); **Notes.** Stoichiometries and sizes are inspired by previous analysis from van Boekel et al. (2005) and Juhász et al. (2010)

Appendix F: Computation of observables

The complex correlated flux $\mathfrak{F}_\nu$ is a linear operator, enabling the addition of those of individual model components. The single-dish spectrum, the correlated flux and the closure phase can be extracted from the complex correlated flux as shown in Buscher (2015).

For this, the observed spatial frequencies $\boldsymbol{q} = (u, v) = (B_x/\lambda,\, B_y/\lambda)$ have to be de-projected to reconstruct a face-on disc by following the steps from Berger & Segransan (2007) and Matter et al. (2014). We apply the counter-clockwise rotation $R(\theta)$ and the scaling matrix $S(i)$ to de-project the spatial frequencies

$$\begin{aligned} q' = q'(i,\theta) &= \|S(i)R(\theta)\boldsymbol{q}\| \\ &= \left\| \begin{pmatrix} \cos(i) & 0 \\ 0 & 1 \end{pmatrix} \begin{pmatrix} \cos(\theta) & -\sin(\theta) \\ \sin(\theta) & \cos(\theta) \end{pmatrix} \begin{pmatrix} u \\ v \end{pmatrix} \right\|. \end{aligned} \tag{F.1}$$

This yields the de-projected spatial frequency $q'(i,\theta)$ with the angle $\psi = \arctan\left(\frac{u'}{v'}\right)$ (polar coordinate representation of $\boldsymbol{q}'$).

To achieve the single-dish spectrum, we take the real part of the complex correlated flux at its 0th spatial frequency, and the modulus for the correlated fluxes:

$$F_\nu = \Re[\mathfrak{F}_\nu(0)], \qquad \text{and} \qquad F_{\nu,\mathrm{corr}} = |\mathfrak{F}_\nu|. \tag{F.2}$$

The phase information can also be extracted from the complex correlated flux. However, turbulence in the atmosphere makes a direct observation of the absolute phases impossible, which is why the closure phases

$$\Phi_{\mathrm{cp},ijk} = \phi_{ij} + \phi_{jk} + \phi_{ki}, \qquad \text{with} \qquad \Phi_{ij} = \phi_{ij} + \epsilon_i - \epsilon_j \tag{F.3}$$

are used. Here, ϕ_{ij} is the real phase between two telescopes, and ϵ_i is the atmospheric aberration per telescope. In a closure triangle, the atmospheric aberrations cancel each other, and the closure phases are computed with the spatial frequencies of the triangle

$$\boldsymbol{q}_{ijk} = \begin{pmatrix} 1 & 0 \\ 0 & 1 \\ 1 & 1 \end{pmatrix} \begin{pmatrix} u_i & v_i \\ u_j & v_j \end{pmatrix}, \quad \text{where} \quad u_k = u_i + u_j. \tag{F.4}$$

Similar as before, we de-project the spatial frequencies with Eq. (F.1) and then compute the closure phases using the bispectrum

$$\Phi_{\mathrm{cp},ijk} = \arg\left(\mathfrak{F}_{ij}\mathfrak{F}_{jk}\mathfrak{F}^*_{ki}\right) = \arg\left(\mathfrak{F}_{ij}\mathfrak{F}_{jk}\mathfrak{F}_{ik}\right). \tag{F.5}$$

Appendix G: Residuals

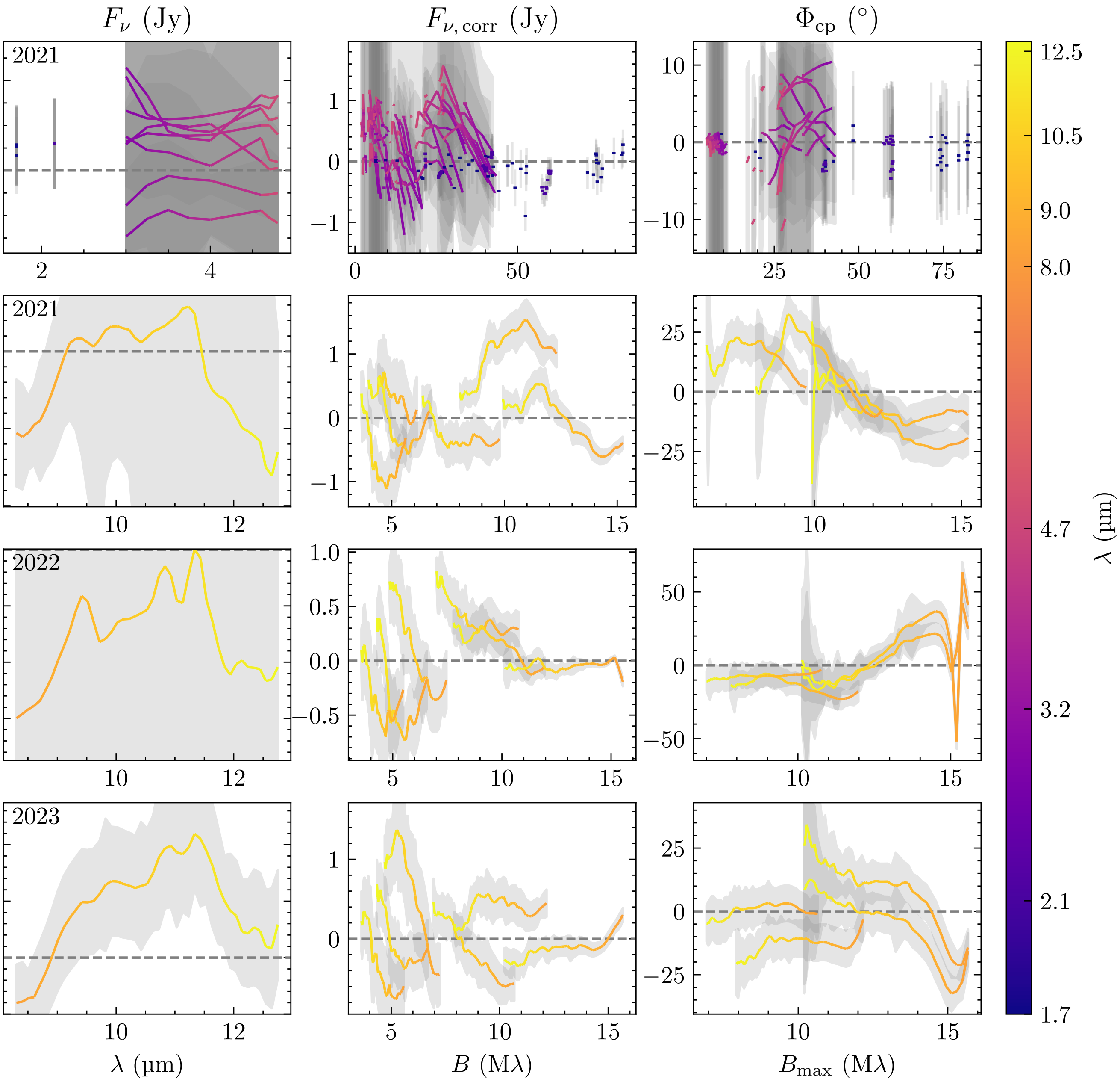

Fig. G.1: Residuals of Fig. 3 with identical layout.